Monthly Notices of the ROYAL ASTRONOMICAL SOCIETY

MNRAS **499,** 6018–6034 (2020) doi:10.1093/mnras/staa3100
Advance Access publication 2020 October 9

Searching for shocks in high-mass starless clump candidates

Feng-Yao Zhu,[1]★ Jun-Zhi Wang,[1] Tie Liu,[1,2] Kee-Tae Kim,[2,3] Qing-Feng Zhu[4] and Fei Li[1]

[1]*Shanghai Astronomical Observatory, Chinese Academy of Sciences, Shanghai 200030, China*
[2]*Korea Astronomy and Space Science Institute, 776 Daedeokdae-ro, Yuseong-gu, Daejeon 34055, Republic of Korea*
[3]*University of Science and Technology, Korea (UST), 217 Gajeong-ro, Yuseong-gu, Daejeon 34113, Republic of Korea*
[4]*CAS Key Laboratory for Research in Galaxies and Cosmology, Department of Astronomy, University of Science and Technology of China, Hefei 230026, China*

Accepted 2020 September 29. Received 2020 August 26; in original form 2020 July 17

ABSTRACT

In order to search for shocks in the very early stage of star formation, we performed single-point surveys of SiO $J = 1$–0, 2–1, and 3–2 lines and the H_2CO $2_{12}-1_{11}$ line towards a sample of 100 high-mass starless clump candidates (SCCs) by using the Korean VLBI Network (KVN) 21-m radio telescopes. The detection rates of the SiO $J = 1$–0, 2–1, 3–2 lines, and the H_2CO line are 31.0, 31.0, 19.5, and 93.0 per cent, respectively. Shocks seem to be common in this stage of massive star formation. The widths of the observed SiO lines [full width at zero power (FWZP)] range from 3.4 to 55.1 km s^{-1}. A significant fraction ($\sim$ 29 per cent) of the detected SiO spectra have broad line widths (FWZP > 20 km s^{-1}), which are very likely associated with fast shocks driven by protostellar outflows. This result suggests that about one third of the SiO-detected SCCs are not really starless but protostellar. On the other hand, about 40 per cent of the detected SiO spectra show narrow line widths (FWZP $<$ 10 km s^{-1}) probably associated with low-velocity shocks which are not necessarily protostellar in origin. The estimated SiO column densities are mostly $0.31-4.32 \times 10^{12}$ cm^{-2}. Comparing the SiO column densities derived from SiO $J = 1$–0 and 2–1 lines, we suggest that the SiO molecules in the SCCs may be in the non-LTE condition. The SiO abundances to H_2 are usually $0.20-10.92 \times 10^{-10}$.

Key words: shock waves – stars: formation – stars: protostars – ISM: structure – radio lines: ISM.

1 INTRODUCTION

Massive starless clumps represent the environments that are in the very early stage of star formation, and are suggested as the first phase of high-mass star formation (Motte, Bontemps & Louvet 2018). They have not been significantly disrupted by feedback from protostars (Matzner 2017; Calahan et al. 2018), and are ideal locations to improve our understanding of massive star and cluster formation (Svoboda et al. 2019). Blind surveys of dust continuum emission at (sub)millimeter wavelengths can be used to detect star-forming regions in different evolutionary stages (Traficante et al. 2015; Csengeri et al. 2016; Svoboda et al. 2016; Urquhart et al. 2018). And a sample of massive clumps have been identified as starless clump candidates (SCCs) in the 1.1-mm continuum Bolocam Galactic Plane Survey (Svoboda et al. 2016). Although there could be undetected low-mass protostars in these regions since only protostars with bolometric luminosities higher than the $30-140 L_{\odot}$ sensitivity of far-infrared Galactic plane surveys are able to be detected, high-mass protostars are unlikely to exist (Svoboda et al. 2016; Calahan et al. 2018). So SCCs can still be representatives of the early stage of star formation since weak feedbacks from low-mass protostars cannot seriously disturb the early star-forming environment. The study of these SCCs can give us a better understanding of the early evolution of star formation. Abundant in star-forming regions, shocks can significantly influence the environments and provide some information of ongoing star formation activities. Surveys of molecular shock tracers towards these SCCs can help us to determine whether the shocks are common in these environments and to study the properties of the shocked materials in the early evolutionary stage of star formation.

SiO lines are often used as a probe of shocks in star-forming regions with a wide range of evolutionary stages (Jiménez-Serra et al. 2010; Duarte-Cabral et al. 2014; Csengeri et al. 2016; Cosentino et al. 2018). SiO is believed to form via sputtering and vapourization of Si atoms from grains due to shock activities (Gusdorf et al. 2008) and its abundance can be enhanced by fast shocks up to six orders of magnitude higher than those of quiescent regions. This makes SiO emission unlikely being contaminated by the line emission from ambient interstellar medium (Li et al. 2019). SiO rotational lines have been observed in various conditions such as high-velocity shocks ($v_s \geq 20$ km s^{-1}) caused by powerful outflows from massive protostars and low-velocity shocks ($v_s < 10$ km s^{-1}) (Nguyen Luong et al. 2013; Duarte-Cabral et al. 2014; Csengeri et al. 2016). Some previous studies reported the observed SiO emission contains both broad and narrow Gaussian components at approximately the same central velocity (Nguyen Luong et al. 2011, 2013; Sanhueza et al. 2013). The broad Gaussian components are commonly attributed to the high-velocity shocks produced by protostellar outflows, while the narrow ones are linked to the low-velocity shocks due to either cloud–cloud collisions or less powerful outflows from low-mass protostars.

★ E-mail: zhufy@shao.ac.cn

The SiO survey towards massive clumps by Csengeri et al. (2016) includes the observations of starless clumps selected from the APEX Telescope Large Area Survey of the Galaxy (ATLASGAL) and a high detection rate of ∼ 61 per cent for SiO (2–1) towards starless clumps is resulted. Li et al. (2019) also observed the SiO (5–4) line towards 201 massive clumps and found a 57 per cent detection rate for the massive clumps in IRDCs. The high detection rates in Csengeri et al. (2016) and Li et al. (2019) seem to suggest that shocks are ubiquitous in the earliest stage of star formation. Moreover, in these samples, more than 25 per cent of starless clumps identified by infrared colour criteria are found associated with broad SiO line profiles due to outflows of deeply embedded high-mass protostars and other starless clumps with narrow SiO components could also contain protostellar objects. This suggests that a large fraction of these SCCs are not actually starless and the SiO lines are very useful to distinguish protostar-embedded clumps and starless clumps. Recently, Svoboda et al. (2019) observed 12 of the most massive SCCs in CO 2–1 and SiO 5–4 lines. Most of these SCCs show bipolar molecular outflows indicating star formation. This also suggests that previous infrared surveys are incomplete to detect embedded protostars with low luminosities. More works are still needed to identify reliable samples of starless sources and to investigate the ubiquity and characteristics of shocks in the previously identified starless clumps.

Besides the information of shocks, the properties of the molecular gas in starless massive clumps can also allow us to understand the early environment of star formation. Formaldehyde, H_2CO, is one of the molecules detected in massive star-forming regions and is widely used to estimate the gas temperature and density (van der Tak et al. 2000; Tang et al. 2017). It is also used as a diagnostic tool to study the star formation in nearby galaxies (Nishimura et al. 2019). The abundance of H_2CO is about 10^{-9}–10^{-10} in the massive star-forming regions (Vichietti et al. 2016).

In this work, we report surveys of the SiO 1–0, 2–1, 3–2 lines, and the H_2CO $2_{12}-1_{11}$ line towards 100 SCCs with Korean VLBI Network (KVN) 21-m telescopes. By using these molecular lines, the ubiquity of shocks and the levels of star formation activities in these SCCs are investigated. The presence of high-velocity and/or low-velocity shocks is also revealed and then the targets with fast shocks due to outflows from protostars can be distinguished from the real starless sources. The organization of this paper is as follows. In Section 2, we describe the observations and the selected sample. The detailed results of the observations are presented in Section 3. The discussions and the analysis about these results are showed in Section 4. In Section 5, the summary is presented.

2 OBSERVATIONS

2.1 Sample

The sample in this study consists of 100 SCCs, which have been observed by Calahan et al. (2018) to search for infall signatures. These targets were bindly selected from the SCC catalogue of Svoboda et al. (2016) with $NH_3(1,1)$ detections. The distances of these sources range from 1.18 to 11.8 kpc and the average and median distances are 4.32 and 4.19 kpc, respectively (Ellsworth-Bowers et al. 2015). The distance distribution of the sample is presented in Fig. 1. About 70 per cent of the sources have distances between 3 and 6 kpc. According to the comparison of the mass and mass surface density between the selected sample and the complete sample of SCCs described in Calahan et al. (2018), the selected sample is representative of the mass range of the complete sample. But, the mass surface densities in the selected sample are on average higher by a factor of ∼2. The v_{LSR} measured from NH_3 observations provided in Svoboda et al. (2016) is regarded as the systemic velocity of each source and used for the current observations.

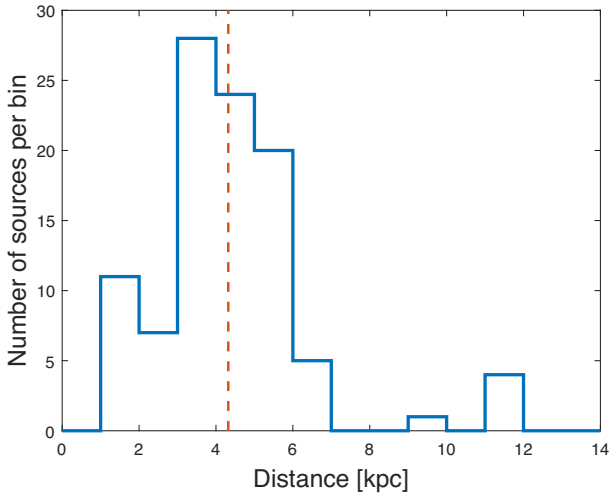

Figure 1. The distance distribution of the sample. The vertical dashed line represents the average distance.

2.2 Observations and data reduction

We conducted single-point molecular line observations using all three (Yonsei, Ulsan and Tamma) KVN 21-m telescopes from 2019 March to June (Kim et al. 2011). All of the 100 sources were observed in the SiO 1–0, 2–1, and H_2CO $2_{12}-1_{11}$ transitions at 43.42376 GHz, 86.84696 GHz, and 140.83950 GHz, respectively. And among the sample, 41 targets were also observed in the SiO 3–2 transition at 130.26861 GHz. The backend was a digital spectrometer that provided 64 MHz bandwidth with 4096 channels and 15.63 kHz frequency channel spacing. The position switching observational mode was used with the reference position of 0.°2 offset from the source in azimuth. The total (ON + OFF) integration times are typically about 1 h for the SiO 1–0 and 2–1 lines. However, we increased the integration time for some marginally detected source to confirm the detection. For the SiO 3–2 line and the H_2CO line, the observation times were commonly about 30 min. The system temperatures range from 80 to 400 K at different frequencies. The FWHM beam sizes of the telescopes are about 63, 34, 23, and 21 arcsec for SiO 1–0, 2–1, 3–2 lines, and H_2CO $2_{12}-1_{11}$ line, respectively. The main beam sizes at the average distance of 4.32 kpc for the four lines are 1.33, 0.72, 0.48, and 0.44 pc and the main beam efficiencies are about 47, 43, 35, and 30, respectively.

Table A1 presents the details of the observations towards individual sources including the rms noise levels and used telescopes. Each source was observed individually with only one telescope except for BGPS 2762, 2931, and 4402. They were observed simultaneously with two telescopes. According to the approximately consistent instrumental parameters of the three KVN 21-m telescopes, the spectra obtained from them are comparable. This was also confirmed by our observations towards W51 E1E2 in the SiO and H_2CO lines. Since the properties of the shocked gas in the SCCs are our main research goals, the SiO lines are more important in this work. In addition, the SiO 2–1 line should provide more representative information than the other SiO lines because it has been observed in more sources than the SiO 3–2 line and its filling factor may be higher than that of the SiO 1–0 line.

The observations were reduced with CLASS reduction package[1]. A linear baseline was removed from each spectrum. The typical rms noise levels of the main-beam brightness temperature scale are about 20 mK for the SiO lines and 40 mK for the H_2CO line at the velocity resolution of about 1 km s^{-1}. However, the levels are significantly lower or higher than the typical ones for some sources because of different integration times or weather conditions. The effect of the variable observing conditions on the detection rates of the SiO lines is discussed in Appendix A. The histograms of the noise levels and the SiO spectra for individual sources are presented in Figs A1 and A2, respectively. By comparing the noise levels between the sources with and without the SiO detections, we find that the SiO detection rates are meaningful.

3 RESULTS

The properties of global dense gas and shocked gas in the SCCs are investigated from the observations. The H_2CO line is used to determine the properties of the dense molecular gas in the SCCs and the SiO lines can help us to study the physical conditions of the shocked gas.

3.1 Detection rates

The H_2CO $2_{12}-1_{11}$ line was detected in 93 targets (93 per cent) with a velocity-integrated intensity ($\int T_{\rm mb}{\rm d}v$) higher than $3\sigma_{\rm area}$, where $\sigma_{\rm area} = \sqrt{N}\Delta v\sigma$ represents the rms noise level of the velocity-integrated intensity. N is the number of channels in the velocity range of the line, Δv means velocity resolution, and σ is rms noise level of a channel. The derived properties of the H_2CO line and the J2000 equatorial of the SCCs are listed in Table 1. In most targets, the line profiles are Gaussian. The line profiles of 10 sources show two velocity components. Four of them have two emission components probably due to the line-of-sight effect since the two emission components are resolved. The other six sources have an absorption component as well as an emission component. These spectra should be due to H_2CO emission at the reference positions. Since these spectra contain false absorption components, they are not included in the calculations of the average spectra presented in Section 3.2. In addition, only the emission components are used to estimate the luminosities, the column densities, and the abundances.

The SiO line profiles are mainly non-Gaussian so that the full width at zero power (FWZP) is used. The FWZP is visually determined as the velocity range where the emission is higher than rms noise level 1σ. The numbers of the detections in the SiO lines are shown in Table 2. The SiO 1–0, 2–1, and 3–2 lines were clearly detected in 31, 31, and 8 sources, respectively. In addition, the numbers of the overlapping detections between the SiO lines are also written in Table 2. There were 28 sources in which both the SiO 1–0 and 2–1 lines were detected. And in eight of them, all the three SiO lines were found. BGPS 2945, 3656, and 4230 were detected only in SiO 1–0 emission. This could be caused by different beam sizes for the SiO 1–0 and 2–1 lines. The region where the SiO lines are emitted may be not very close to the centre of beam and covered only by the observation at 43.4 GHz. On the other hand, BGPS 3247, 4297, and 4375 were detected only in SiO 2–1 emission. This could be because the SiO emission region is compact. For compact emission, the different beam sizes for the two SiO lines would favour the detection of the SiO 2–1 line because the greater beam dilution effect at 43.4 GHz would potentially reduce the observed SiO 1–0 emission below the instrumental sensitivity limit. The detection rates of the SiO 1–0 and 2–1 lines are both 31 per cent. This indicates that shocks are common in SCCs. The star formation activities seem to be abundant even at the very early evolutionary age if the shocks are attributed to outflows from protostellar structures. The large distance range from 1.18–11.8 kpc may lead to a bias in the detection rates. This was checked by using Spearman test relation between detection rates of the SiO 1–0 and 2–1 lines and the distances of the sources. The sources are divided into several groups according to their distances and the correlations between detection rate and distance are tested. But the p-values for the SiO 1–0 and 2–1 lines are 38 and 73 per cent, respectively. This result suggests that the correlations are not significant.

3.2 Line width

The FWZPs of the detected SiO 1–0 and 2–1 lines are listed in Table 3. Following Beuther & Sridharan (2007), the SiO spectra are divided into three groups as low velocity (FWZP $<$ 10 km s^{-1}), intermediate velocity (10 $\leq$ FWZP $<$ 20 km s^{-1}) and high velocity (FWZP $\geq$ 20 km s^{-1}). For the SiO 1–0 line, there are 13 sources in the low-velocity group, 11 sources in the intermediate-velocity group, and 7 sources in the high-velocity group. For the SiO 2–1 line, the corresponding numbers are 14, 12, and 5, respectively. The mean FWZPs are 14.88 and 11.59 km s^{-1} for the SiO 1–0 and 2–1 lines and the median values are 11.75 and 10.50 km s^{-1}, respectively. The histograms of FWZPs are displayed in Fig. 2. More than half of the sources have FWZPs $>$ 10 km s^{-1} probably attributed to outflows from undetected embedded protostars while the number of the sources associated with narrow velocity ranges (FWZP $<$ 10 km s^{-1}) is still considerable. In this work, the proportions of sources in the low-velocity group are $\sim$ 40 per cent for both SiO lines. The comparison of the FWZP values for the SiO 1–0 and 2–1 lines is presented in Fig. 3. The relation between the FWZPs of the two SiO lines is obvious. The mean and median FWZPs of the two SiO lines are roughly equal although the covered regions in the observations of the SiO 1–0 and 2–1 lines are different due to the different beam sizes. Other detailed properties of the SiO lines are also written in Table 3.

The SiO line profiles of most sources do not have high signal-to-noise ratios so that the high-velocity wings cannot be clearly distinguished from noise for individual sources. The average line profiles of the SiO 1–0 and 2–1 emission from detected sources located between 2–7 kpc are presented in Fig. 4. The value of main beam temperature is adjusted as if the distances of these sources are uniformly 1 kpc. The detected sources with a large distance $>$7 kpc are excluded lest the spectra of the most distant sources dominate the average spectra. Single Gaussians are fitted to the average spectra and the fitted curves are also presented. The fitted curve to the SiO 1–0 spectrum has a 6.8 km s^{-1} FWHM and the high-velocity wings are also shown. The FWHM of the fitted curve to the SiO 2–1 spectrum is 9.4 km s^{-1}. In addition, the distance-weighted average SiO line profiles from the sources without clear detections are plotted in Fig. 5. The profiles suggest that the SiO emission is undetected in these sources mainly due to intrinsic property and not because of the instrumental sensitivity limit.

The widths of the SiO 3–2 transition are provided in Table 4. The mean and median values of the FWZPs for the SiO 3–2 line are 8.46 and 8.0 km s^{-1}, respectively. There is no source with FWZP $>$ 20 km s^{-1} and almost all of the sources associated with broad SiO 1–0 and 2–1 line profiles are not detected in the SiO 3–2 line. It

[1] http://www.iram.fr/IRAMFR/GILDAS

Table 1. The properties of the H_2CO $2_{12}-1_{11}$ line. $V_{lsr}(NH_3)$ and $V_{lsr}(H_2CO)$ are line central velocities. The $\int T_{mb}dv$ is velocity-integrated intensity. T_{mb} is the line peak at main beam temperature. FWHM is full width at half-maximum. L_{H_2CO} is luminosity. $N(H_2CO)$ and $X(H_2CO)$ are column density and abundance, respectively.

Name	RA	Dec.	$V_{lsr}(NH_3)/V_{lsr}(H_2CO)$ ($km\,s^{-1}$)	$\int T_{mb}dv$ ($K\,km\,s^{-1}$)	T_{mb} (K)	FWHM ($km\,s^{-1}$)	L_{H_2CO} ($10^{-7}L_\odot$)	$N(H_2CO)$ (cm^{-2})	$X(H_2CO)$
BGPS 2427	18:09:33.88	–20:47:00.76	30.66 ± 0.65/...	–	–	–	–	–	–
BGPS 2430	18:08:49.41	–20:40:23.82	21.27 ± 1.19/...	–	–	–	–	–	–
BGPS 2432	18:09:44.59	–20:47:10.21	31.08 ± 0.71/...	–	–	–	–	–	–
BGPS 2437	18:10:19.41	–20:50:27.45	−1.87 ± 0.56/27.61 ± 0.46	1.066 ± 0.195	0.23	3.47 ± 0.82	145.48	5.01×10^{12}	8.76×10^{-10}
BGPS 2533	18:10:30.29	–20:14:44.20	31.84 ± 0.41/...	–	–	–	–	–	–
BGPS 2564	18:10:06.08	–18:46:05.64	29.57 ± 0.27/29.21 ± 0.05	0.480 ± 0.045	0.35	0.98 ± 0.12	30.23	1.94×10^{12}	6.67×10^{-10}
BGPS 2693	18:11:13.56	–17:44:54.85	19.13 ± 0.21/19.08 ± 0.06	1.379 ± 0.133	0.86	1.17 ± 0.15	42.40	5.65×10^{12}	1.45×10^{-9}
BGPS 2710	18:13:49.04	–17:59:33.25	34.59 ± 0.42/34.40 ± 0.11	3.219 ± 0.608	1.13	2.74 ± 0.39	32.10	1.38×10^{13}	1.74×10^{-9}
			35.21 ± 0.36	−3.853 ± 0.240	−0.80	5.25 ± 0.60			
BGPS 2724	18:14:13.61	–17:59:52.02	36.25 ± 1.43/35.68 ± 0.14	4.404 ± 0.303	0.80	4.03 ± 0.31	42.83	2.24×10^{13}	8.09×10^{-9}
BGPS 2732	18:14:26.85	–17:58:50.93	37.47 ± 0.85/36.23 ± 0.14	1.560 ± 0.100	0.29	4.14 ± 0.39	15.33	9.70×10^{12}	8.51×10^{-9}
BGPS 2742	18:14:29.10	–17:57:21.83	36.01 ± 1.16/40.08 ± 1.01	3.833 ± 0.543	0.20	13.92 ± 2.00	37.16	2.08×10^{13}	1.27×10^{-8}
BGPS 2762	18:11:39.52	–17:32:09.40	17.85 ± 0.69/18.37 ± 0.05	3.494 ± 0.188	1.31	2.10 ± 0.15	264.11	1.86×10^{13}	3.79×10^{-9}
BGPS 2931	18:17:27.51	–17:06:08.42	22.77 ± 0.26/22.97 ± 0.08	3.005 ± 0.231	0.86	2.44 ± 0.22	224.55	1.21×10^{13}	3.33×10^{-9}
BGPS 2940	18:17:17.15	–17:01:07.47	20.04 ± 0.92/19.85 ± 0.02	10.088 ± 0.100	2.21	3.71 ± 0.04	791.58	4.81×10^{13}	5.83×10^{-9}
BGPS 2945	18:17:27.35	–17:00:23.66	22.68 ± 0.25/22.68 ± 0.04	1.939 ± 0.096	0.90	1.68 ± 0.13	18.64	7.81×10^{12}	1.30×10^{-9}
BGPS 2949	18:17:33.74	–16:59:34.94	22.52 ± 0.33/21.64 ± 0.06	2.504 ± 0.108	0.61	3.21 ± 0.12	28.36	1.01×10^{13}	2.21×10^{-9}
BGPS 2970	18:17:05.08	–16:43:28.66	40.01 ± 0.62/40.23 ± 0.07	1.820 ± 0.115	0.58	2.43 ± 0.20	160.41	7.69×10^{12}	7.69×10^{-10}
BGPS 2971	18:16:48.12	–16:41:08.91	36.55 ± 0.47/39.22 ± 0.31	3.333 ± 0.294	0.39	6.05 ± 0.65	76.05	1.49×10^{13}	5.48×10^{-9}
BGPS 2976	18:17:07.84	–16:41:14.59	39.63 ± 0.37/39.63 ± 0.07	1.623 ± 0.091	0.45	2.45 ± 0.17	37.64	6.89×10^{12}	1.59×10^{-9}
BGPS 2984	18:18:18.23	–16:44:52.26	18.42 ± 0.22/19.28 ± 0.13	0.256 ± 0.050	0.19	0.99 ± 0.26	6.11	1.03×10^{12}	2.10×10^{-10}
BGPS 2986	18:18:29.68	–16:44:50.69	19.97 ± 0.31/20.28 ± 0.05	3.386 ± 0.170	1.38	1.75 ± 0.15	95.16	1.36×10^{13}	9.38×10^{-10}
BGPS 3018	18:19:13.88	–16:35:16.47	18.96 ± 0.47/18.93 ± 0.04	1.904 ± 0.075	0.78	1.80 ± 0.10	560.64	8.01×10^{12}	1.21×10^{-9}
BGPS 3030	18:19:19.68	–16:31:39.82	19.01 ± 0.28/19.10 ± 0.02	2.330 ± 0.079	0.96	1.73 ± 0.07	51.35	1.09×10^{13}	1.62×10^{-9}
BGPS 3110	18:20:16.27	–16:08:51.13	17.69 ± 0.91/17.32 ± 0.03	19.574 ± 0.331	3.85	3.70 ± 0.07	545.00	1.16×10^{14}	6.74×10^{-9}
BGPS 3114	18:20:31.50	–16:08:37.80	.../22.87 ± 0.02	7.185 ± 0.079	1.58	3.36 ± 0.04	169.96	2.99×10^{13}	5.08×10^{-10}
BGPS 3117	18:20:06.68	–16:04:45.75	18.57 ± 0.74/18.67 ± 0.03	3.928 ± 0.108	1.25	2.29 ± 0.07	108.93	2.91×10^{13}	5.18×10^{-9}
BGPS 3118	18:20:16.17	–16:05:50.72	17.21 ± 0.76/16.88 ± 0.02	11.025 ± 0.160	3.20	2.71 ± 0.05	305.75	6.26×10^{13}	6.69×10^{-9}
BGPS 3125	18:20:06.11	–16:01:58.02	21.53 ± 0.34/21.39 ± 0.03	4.508 ± 0.123	1.51	2.36 ± 0.10	375.06	2.39×10^{13}	4.59×10^{-9}
BGPS 3128	18:20:35.27	–16:04:53.81	19.75 ± 0.76/18.36 ± 0.06	9.840 ± 0.429	2.54	3.08 ± 0.15	1185.1	5.20×10^{13}	5.92×10^{-9}
BGPS 3129	18:20:12.99	–16:00:24.13	19.72 ± 0.49/19.41 ± 0.04	3.084 ± 0.149	1.13	1.99 ± 0.13	392.96	1.48×10^{13}	4.81×10^{-9}
BGPS 3134	18:19:52.72	–15:56:01.56	20.47 ± 0.59/20.95 ± 0.01	3.970 ± 0.050	1.70	1.70 ± 0.02	458.40	1.79×10^{13}	1.11×10^{-9}
BGPS 3139	18:20.34.24	–15:58.14.00	21.80 ± 0.37/20.12 ± 0.01	6.884 ± 0.041	2.31	2.17 ± 0.02	1394.5	3.23×10^{13}	4.17×10^{-9}
BGPS 3151	18:20:23.19	–15:39:31.96	39.40 ± 0.37/15.50 ± 0.04	0.646 ± 0.038	0.35	1.38 ± 0.09	102.43	7.94×10^{12}	7.63×10^{-10}
			39.82 ± 0.05	1.295 ± 0.050	0.39	2.49 ± 0.12			
BGPS 3220	18:24:57.03	–13:20:32.39	46.13 ± 1.76/46.79 ± 0.05	6.001 ± 0.184	1.09	4.33 ± 0.14	623.76	2.93×10^{13}	2.99×10^{-9}
BGPS 3243	18:25:32.74	–13:01:31.05	68.47 ± 0.31/50.61 ± 0.13	−1.196 ± 0.124	−0.35	2.52 ± 0.29	194.50	5.36×10^{12}	5.84×10^{-10}
			68.23 ± 0.20	1.329 ± 0.199	0.33	3.09 ± 0.77			
BGPS 3247	18:25:14.45	–12:54:16.74	45.17 ± 0.35/45.00 ± 0.06	1.759 ± 0.120	0.68	1.88 ± 0.16	240.85	7.31×10^{12}	1.75×10^{-9}
BGPS 3276	18:26:24.92	–12:49:30.07	67.38 ± 0.71/67.00 ± 0.15	1.134 ± 0.124	0.26	2.77 ± 0.32	89.60	5.31×10^{12}	1.57×10^{-9}
BGPS 3300	18:26:28.42	–12:37:03.98	64.15 ± 1.04/64.17 ± 0.19	1.701 ± 0.170	0.33	3.71 ± 0.38	1604.0	7.56×10^{12}	3.44×10^{-9}
BGPS 3302	18:27:15.23	–12:42:56.45	66.37 ± 0.75/66.57 ± 0.09	4.470 ± 0.158	0.64	5.10 ± 0.20	4300.4	2.19×10^{13}	2.73×10^{-9}
BGPS 3306	18:23:34.02	–12:13:52.79	57.11 ± 0.36/57.16 ± 0.07	0.965 ± 0.091	0.48	1.46 ± 0.18	152.64	3.93×10^{12}	1.13×10^{-9}
BGPS 3312	18:25:44.52	–12:28:34.11	47.30 ± 0.30/47.10 ± 0.08	0.883 ± 0.084	0.39	1.90 ± 0.22	169.91	4.23×10^{12}	2.15×10^{-9}
BGPS 3315	18:25:33.24	–12:26:50.63	44.31 ± 0.68/47.29 ± 0.10	2.761 ± 0.178	0.64	3.16 ± 0.25	439.44	1.38×10^{13}	1.70×10^{-9}
BGPS 3344	18:26:40.00	–12:25:15.81	65.69 ± 0.36/47.09 ± 0.17	−1.243 ± 0.211	−0.39	2.35 ± 0.53	180.24	6.35×10^{12}	1.28×10^{-9}
			65.53 ± 0.34	1.399 ± 0.249	0.26	3.86 ± 0.89			
BGPS 3442	18:28:13.51	–11:40:44.94	65.75 ± 0.46/66.88 ± 0.32	1.319 ± 0.153	0.19	5.06 ± 0.77	108.16	5.43×10^{12}	1.05×10^{-9}
BGPS 3444	18:28:27.26	–11:41:33.99	69.69 ± 0.44/...	–	–	–	–	–	–
BGPS 3475	18:28:28.28	–11:06:44.16	75.86 ± 1.18/77.19 ± 0.30	0.828 ± 0.145	0.18	3.41 ± 0.63	67.25	3.93×10^{12}	1.37×10^{-10}
BGPS 3484	18:29:15.74	–10:58:28.73	56.35 ± 0.89/56.03 ± 0.33	1.408 ± 0.236	0.23	4.44 ± 0.86	118.30	6.85×10^{12}	3.89×10^{-9}
BGPS 3487	18:29:22.77	–10:58:01.69	54.60 ± 1.22/55.70 ± 0.13	2.214 ± 0.141	0.39	4.24 ± 0.30	186.71	1.48×10^{13}	7.67×10^{-9}
BGPS 3534	18:30:33.45	–10:24:19.00	65.06 ± 0.99/...	–	–	–	–	–	–
BGPS 3604	18:30:43.92	–9:34:42.15	51.52 ± 0.44/51.32 ± 0.06	2.396 ± 0.134	0.78	2.45 ± 0.17	2011.5	9.69×10^{12}	1.73×10^{-9}
BGPS 3606	18:29:41.95	–9:24:49.10	49.56 ± 0.42/49.49 ± 0.16	0.443 ± 0.083	0.20	1.60 ± 0.30	54.50	1.74×10^{12}	5.16×10^{-10}
BGPS 3608	18:31:54.82	–9:39:05.03	63.77 ± 1.36/63.96 ± 0.27	1.995 ± 0.220	0.26	5.45 ± 0.62	230.13	8.45×10^{12}	1.85×10^{-9}
BGPS 3627	18:31:42.32	–9:24:29.17	81.30 ± 0.51/82.25 ± 0.54	0.596 ± 0.149	0.11	3.99 ± 1.05	71.83	2.45×10^{12}	7.18×10^{-10}
BGPS 3656	18:32:49.54	–9:21:29.26	77.25 ± 0.79/27.91 ± 0.29	0.749 ± 0.141	0.19	2.89 ± 0.74	79.14	3.04×10^{12}	8.49×10^{-10}
BGPS 3686	18:34:14.58	–9:18:35.84	77.28 ± 0.50/78.14 ± 0.29	1.979 ± 0.199	0.24	5.92 ± 0.69	118.35	8.61×10^{12}	1.43×10^{-9}
BGPS 3705	18:34:32.69	–9:14:09.40	61.58 ± 0.90/74.42 ± 0.57	5.559 ± 0.303	0.19	21.00 ± 1.23	373.78	2.31×10^{13}	4.90×10^{-9}
BGPS 3710	18:34:20.55	–9:10:01.94	74.68 ± 1.04/75.11 ± 0.13	3.014 ± 0.195	0.45	4.85 ± 0.47	130.96	1.30×10^{13}	2.09×10^{-9}
BGPS 3716	18:34:24.15	–9:08:03.60	75.87 ± 1.57/76.81 ± 0.12	3.738 ± 0.149	0.48	5.83 ± 0.26	256.25	1.73×10^{13}	5.67×10^{-9}
BGPS 3736	18:33:28.22	–8:55:04.36	65.39 ± 0.71/65.74 ± 0.06	1.544 ± 0.095	6.44	1.70 ± 0.10	270.75	6.43×10^{12}	1.44×10^{-9}
BGPS 3822	18:33:32.06	–8:32:26.27	54.55 ± 0.64/54.86 ± 0.10	1.909 ± 0.158	0.51	2.71 ± 0.26	150.15	7.70×10^{12}	8.56×10^{-10}
BGPS 3833	18:33:36.50	–8:30:50.70	55.59 ± 0.55/55.23 ± 0.30	0.903 ± 0.156	0.19	3.59 ± 0.85	126.16	7.53×10^{12}	1.29×10^{-9}
			81.71 ± 0.33	0.953 ± 0.156	0.19	4.17 ± 0.84			
BGPS 3892	18:35:59.74	–8:38:56.48	64.46 ± 0.95/63.33 ± 0.13	0.531 ± 0.080	0.23	1.63 ± 0.28	103.48	2.13×10^{12}	1.76×10^{-10}
BGPS 3922	18:33:40.98	–8:14:55.30	89.22 ± 0.48/89.28 ± 0.12	0.578 ± 0.080	0.26	1.75 ± 0.29	3897.1	2.36×10^{12}	6.15×10^{-10}
BGPS 3924	18:34:51.17	–8:23:40.02	81.29 ± 0.87/81.35 ± 0.14	0.440 ± 0.073	0.23	1.59 ± 0.29	101.84	1.78×10^{12}	5.55×10^{-10}
BGPS 3982	18:34:30.79	–8:02:07.36	53.94 ± 0.32/54.28 ± 0.15	1.640 ± 0.145	0.39	3.47 ± 0.35	1523.8	6.81×10^{12}	2.01×10^{-9}
BGPS 4029	18:35:54.40	–7:59:44.60	81.52 ± 0.77/81.43 ± 0.30	2.179 ± 0.409	0.55	3.05 ± 0.53	188.95	8.81×10^{12}	9.13×10^{-10}
BGPS 4082	18:35:10.07	–7:39:43.55	99.52 ± 0.51/99.83 ± 0.40	4.683 ± 0.631	0.61	6.04 ± 1.09	838.26	1.99×10^{13}	3.90×10^{-9}
BGPS 4095	18:35:04.00	–7:36:06.46	112.99 ± 0.44/118.07 ± 0.24	1.120 ± 0.344	0.48	1.84 ± 0.94	222.38	4.74×10^{12}	6.90×10^{-10}
BGPS 4119	18:36:29.65	–7:42:06.09	55.33 ± 1.20/55.36 ± 0.17	2.223 ± 0.136	0.29	5.42 ± 0.40	478.76	9.86×10^{12}	4.65×10^{-9}
BGPS 4135	18:37:44.06	–7:48:15.35	59.63 ± 1.71/58.39 ± 0.07	0.708 ± 0.066	0.29	1.70 ± 0.20	109.59	5.39×10^{12}	1.20×10^{-9}
			61.72 ± 0.11	0.534 ± 0.070	0.19	1.93 ± 0.35			
BGPS 4140	18:36:49.66	–7:40:36.83	96.00 ± 0.40/96.03 ± 0.14	0.969 ± 0.178	0.35	1.73 ± 0.43	87.79	4.29×10^{12}	1.39×10^{-9}
BGPS 4145	18:36:52.95	–7:39:49.20	96.53 ± 0.52/96.44 ± 0.12	0.514 ± 0.111	0.35	1.02 ± 0.25	88.43	2.21×10^{12}	5.74×10^{-10}

Table 1 – *continued*

Name	RA	Dec.	$V_{lsr}(NH_3)/V_{lsr}(H_2CO)$ (km s^{-1})	$\int T_{mb}dv$ (K km s^{-1})	T_{mb} (K)	FWHM (km s^{-1})	L_{H_2CO} ($10^{-7}L_\odot$)	$N(H_2CO)$ (cm^{-2})	$X(H_2CO)$
			101.44 ± 0.14	−2.661 ± 0.208	−0.55	3.56 ± 0.33			
BGPS 4191	18:37:04.58	–7:33:12.26	97.51 ± 0.56/97.14 ± 0.14	1.639 ± 0.174	0.45	2.61 ± 0.30	298.01	6.85×10^{12}	1.17×10^{-9}
BGPS 4230	18:35:50.85	–7:12:23.58	107.44 ± 0.50/107.42 ± 0.08	1.341 ± 0.091	0.45	2.18 ± 0.08	235.36	6.18×10^{12}	8.06×10^{-10}
BGPS 4294	18:38:51.58	–6:55:36.52	56.17 ± 0.56/56.39 ± 0.11	1.780 ± 0.100	0.33	4.17 ± 0.26	398.71	7.88×10^{12}	1.79×10^{-9}
BGPS 4297	18:38:56.37	–6:55:08.44	58.65 ± 0.56/58.60 ± 0.21	1.224 ± 0.318	0.35	2.67 ± 0.93	209.50	6.23×10^{12}	2.10×10^{-9}
			63.72 ± 0.60	−1.178 ± 0.275	−0.19	4.48 ± 1.19			
BGPS 4346	18:38:49.58	–6:31:27.06	92.59 ± 1.71/93.35 ± 0.09	4.450 ± 0.133	0.51	6.24 ± 0.19	1045.3	2.80×10^{13}	1.96×10^{-8}
BGPS 4347	18:38:42.93	–6:30:27.83	93.47 ± 0.82/93.66 ± 0.06	3.523 ± 0.100	0.61	4.13 ± 0.14	684.06	1.58×10^{13}	5.72×10^{-9}
BGPS 4354	18:38:51.42	–6:29:15.38	93.97 ± 0.86/92.97 ± 0.97	2.795 ± 0.608	0.26	9.19 ± 2.46	660.38	1.16×10^{13}	3.20×10^{-9}
BGPS 4356	18:37:29.48	–6:18:12.13	109.94 ± 0.72/110.83 ± 0.29	2.669 ± 0.371	0.51	4.20 ± 0.64	366.49	1.20×10^{13}	1.18×10^{-9}
BGPS 4375	18:39:10.19	–6:21:15.90	93.07 ± 0.42/93.21 ± 0.12	0.965 ± 0.199	0.45	1.56 ± 0.54	96.23	3.90×10^{12}	8.59×10^{-10}
BGPS 4396	18:38:34.74	–5:56:43.97	112.73 ± 0.47/97.02 ± 0.29	0.894 ± 0.166	0.23	2.88 ± 0.59	165.93	9.04×10^{12}	8.14×10^{-10}
			113.30 ± 0.26	1.316 ± 0.240	0.29	3.50 ± 1.02			
BGPS 4402	18:39:28.64	–5:57:58.57	99.21 ± 0.59/99.17 ± 0.21	1.391 ± 0.145	0.23	4.46 ± 0.63	177.00	5.80×10^{12}	9.31×10^{-10}
			113.93 ± 0.29	−0.845 ± 0.119	−0.16	4.65 ± 0.64			
BGPS 4422	18:38:47.88	–5:36:16.38	110.71 ± 0.46/110.83 ± 0.16	0.835 ± 0.100	0.23	3.05 ± 0.49	91.38	3.59×10^{12}	9.60×10^{-10}
BGPS 4472	18:41:17.32	–5:09:56.83	46.88 ± 0.40/47.71 ± 0.08	3.419 ± 0.100	0.41	6.10 ± 0.23	244.90	1.48×10^{13}	2.57×10^{-9}
BGPS 4732	18:44:23.40	–4:02:01.21	88.32 ± 0.54/88.20 ± 0.14	1.458 ± 0.133	0.33	3.17 ± 0.33	144.33	5.96×10^{12}	5.62×10^{-10}
BGPS 4827	18:44:42.45	–3:44:21.63	86.10 ± 0.50/86.30 ± 0.07	2.198 ± 0.124	0.64	2.48 ± 0.18	369.51	9.91×10^{12}	9.92×10^{-10}
BGPS 4841	18:42:15.65	–3:22:26.19	83.98 ± 0.66/83.40 ± 0.10	1.188 ± 0.104	0.39	2.29 ± 0.23	149.66	4.83×10^{12}	7.88×10^{-10}
BGPS 4902	18:46:11.36	–3:42:55.73	84.14 ± 1.05/84.12 ± 0.07	4.078 ± 0.145	0.74	3.98 ± 0.17	612.16	1.73×10^{13}	3.93×10^{-9}
BGPS 4953	18:45:51.82	–3:26:24.16	90.78 ± 0.77/90.89 ± 0.11	1.759 ± 0.116	0.41	3.14 ± 0.26	368.68	7.25×10^{12}	2.03×10^{-9}
BGPS 4962	18:45:59.61	–3:25:14.53	88.31 ± 0.39/88.87 ± 0.25	1.354 ± 0.215	0.33	3.10 ± 0.56	347.76	5.56×10^{12}	1.57×10^{-9}
BGPS 4967	18:43:27.80	–3:05:14.94	80.31 ± 0.54/80.80 ± 0.09	0.891 ± 0.165	0.61	1.06 ± 5.33	83.70	3.63×10^{12}	7.30×10^{-10}
BGPS 5021	18:44:37.07	–2:55:04.40	80.05 ± 0.65/79.86 ± 0.13	2.653 ± 0.169	0.48	4.29 ± 0.33	192.28	1.08×10^{13}	1.27×10^{-9}
BGPS 5064	18:45:48.44	–2:44:31.65	100.72 ± 0.59/100.80 ± 0.10	2.873 ± 0.199	0.58	3.64 ± 0.37	539.90	1.29×10^{13}	2.70×10^{-9}
BGPS 5089	18:48:49.88	–2:59:47.86	85.20 ± 0.64/85.54 ± 0.07	1.724 ± 0.100	0.55	2.53 ± 0.18	509.91	7.59×10^{12}	1.28×10^{-9}
BGPS 5090	18:46:35.81	–2:42:30.19	96.30 ± 0.64/96.83 ± 0.11	0.803 ± 0.111	0.41	1.54 ± 0.25	149.05	3.21×10^{12}	7.97×10^{-10}
BGPS 5114	18:50:23.54	–3:01:31.58	65.82 ± 0.76/64.51 ± 0.35	2.275 ± 0.283	0.35	5.33 ± 0.69	213.46	9.75×10^{12}	1.39×10^{-9}
BGPS 5166	18:47:54.26	–2:26:07.11	102.73 ± 0.53/102.40 ± 0.06	2.175 ± 0.145	0.93	1.86 ± 0.14	559.08	9.68×10^{12}	2.42×10^{-9}
BGPS 5183	18:47:00.29	–2:16:38.63	113.78 ± 0.44/...	–	–	–	–	–	–
BGPS 5243	18:47:54.70	–2:11:10.72	95.89 ± 0.44/96.06 ± 0.13	1.170 ± 0.153	0.45	2.12 ± 0.35	219.85	4.83×10^{12}	1.02×10^{-9}

Table 2. The numbers of overlapping detections between the SiO and H_2CO lines. The numbers in the diagonal represent the total numbers of the detections in the corresponding lines.

	SiO 1–0	SiO 2–1	SiO 3–2	H_2CO
SiO 1–0	31	28	8	31
SiO 2–1	28	31	8	31
SiO 3–2	8	8	8	8
H_2CO	31	31	8	93

could be caused by the low sensitivity limitation in the SiO 3–2 observations since the noise of the SiO 3–2 spectrum is higher than those of the SiO 1–0 and 2–1 spectra in most of these sources. But the different beam sizes can also be a factor. The conclusion cannot be made before mapping observations are performed.

The FWHMs of the H_2CO lines are included in Table 1. The average value of the FWHMs of the H_2CO lines is 3.47 km s^{-1} and the median value is 3.05 km s^{-1}. The average H_2CO line profile is also calculated and displayed in the top panel of Fig. 6. The comparison between the distance-weighted average H_2CO line profiles from the sources with and without SiO emissions is displayed in the lower panel. The FWHMs of the average H_2CO line profiles from the sources associated with SiO emissions and without SiO emissions are 3.46 and 2.79 km s^{-1}, respectively. But the difference of the two average FWHMs is not statistically significant. The line widths of the SiO and H_2CO molecules cannot be explained by thermal broadenings with reasonable temperature of dense gases. So the higher values of the line widths are mostly attributed to turbulence or bulk motions. The significant difference in the velocity fields showed from line widths between SiO and H_2CO emissions suggests the different origins and distributions between these two molecules.

3.3 Luminosity

Since the spatial distributions of the gases that emit the molecular lines are not known, we use fluxes per beam calculated from velocity-integrated intensity to estimate the luminosities of the SiO and H_2CO lines for simplicity. So the derived values represent the lower limit of the real luminosities. In Table 3, the luminosities of the SiO 1–0 and 2–1 lines are listed. And those of the SiO 3–2 line and the H_2CO line are provided in Table 4 and 1, respectively. The luminosity ranges from 0.26×10^{-7} to $1.38 \times 10^{-5} L_\odot$ for the SiO 1–0 line, from 1.98×10^{-7} to $3.17 \times 10^{-5} L_\odot$ for the SiO 2–1 line, from 8.75×10^{-7} to $9.46 \times 10^{-6} L_\odot$ for the SiO 3–2 line, and 6.11×10^{-7} to $4.30 \times 10^{-4} L_\odot$ for the H_2CO line. The median values of the luminosities are 9.28×10^{-7}, 3.20×10^{-6}, 2.32×10^{-6}, and $1.89 \times 10^{-5} L_\odot$ for the corresponding lines, respectively.

3.4 SiO column density and abundance

Under the assumption of a beam-filling factor of unity and a LTE condition for the SiO 1–0 and 2–1 lines and the optically thin assumption, the molecular column density can be derived by the equation below (Mangum & Shirley 2015)

$$N = \frac{3h}{8\pi^3 S\mu^2} \frac{Q_{rot}(T_{ex})}{g_j g_k g_s} \frac{\exp(E_u/kT_{ex})}{\exp(h\nu/kT_{ex}) - 1} \frac{\int T_{mb} dv}{J_\nu(T_{ex}) - J_\nu(T_{bg})}, \quad (1)$$

where h is the Planck constant, S is the line strength, and μ is the dipole moment. $Q_{rot}(T_{ex})$ is the partition function for the excitation temperature T_{ex}. $T_{bg} = 2.73$ K is the temperature of the background radiation. $g_J = 2J_u + 1$ is the rotational degeneracy, and $g_K = 1$ and $g_s = 1$ are the K degeneracy and spin degeneracy for SiO molecules, respectively. $J_\nu(T) = \frac{h\nu}{k}(\exp(h\nu/kT) - 1)^{-1}$ is the Rayleigh–Jeans brightness temperature.

The median gas kinetic temperature of these SCCs is 14 K (Svoboda et al. 2016), but the temperature of the shocked gas should

Table 3. The properties of the SiO 1–0 and 2–1 lines emitted from corresponding sources. FWZP is full width at zero power. L_{SiO1-0} and L_{SiO2-1} are the luminosities for the SiO 1–0 and 2–1 lines, respectively.

Name	SiO 1–0					SiO 2–1				
	V_{lsr} (km s^{-1})	$\int T_{mb} dv$ (K km s^{-1})	T_{mb} (K)	FWZP (km s^{-1})	L_{SiO1-0} $10^{-7} L_{\odot}$	V_{lsr} (km s^{-1})	$\int T_{mb} dv$ (K km s^{-1})	T_{mb} (K)	FWZP (km s^{-1})	L_{SiO2-1} ($10^{-7} L_{\odot}$)
BGPS 2724	34.15 ± 0.40	0.098 ± 0.028	0.049	3.5	0.26	34.80 ± 0.76	0.243 ± 0.055	0.049	7.9	1.98
BGPS 2945	20.85 ± 0.28	0.201 ± 0.035	0.080	6.1	0.43	–	–	–	–	–
BGPS 2970	40.81 ± 0.84	0.688 ± 0.088	0.061	25.9	13.04	43.03 ± 1.84	0.324 ± 0.065	0.061	7.2	26.89
BGPS 2976	40.78 ± 1.05	0.420 ± 0.061	0.041	19.0	1.61	40.03 ± 1.84	0.403 ± 0.066	0.026	22.6	6.10
BGPS 3110	17.96 ± 0.25	0.604 ± 0.061	0.131	8.5	4.18	17.48 ± 0.18	0.935 ± 0.070	0.170	13.7	12.58
BGPS 3114	22.27 ± 0.50	0.355 ± 0.053	0.068	10.0	2.29	22.69 ± 0.27	0.548 ± 0.053	0.115	8.6	7.69
BGPS 3118	18.18 ± 0.75	0.430 ± 0.056	0.045	20.7	2.39	18.06 ± 0.59	0.659 ± 0.078	0.070	15.6	13.00
BGPS 3128	17.84 ± 0.56	0.268 ± 0.048	0.061	8.6	8.71	18.22 ± 0.47	0.404 ± 0.081	0.093	7.0	29.31
BGPS 3139	19.76 ± 0.34	0.163 ± 0.026	0.064	5.3	8.33	19.84 ± 0.85	0.141 ± 0.035	0.026	7.0	16.88
BGPS 3220	46.34 ± 0.20	0.205 ± 0.035	0.086	7.0	5.15	44.77 ± 0.45	0.345 ± 0.056	0.100	5.6	23.48
BGPS 3247	–	–	–	–	–	45.41 ± 0.48	0.555 ± 0.075	0.115	7.7	67.19
BGPS 3344	62.09 ± 2.34	0.258 ± 0.056	0.019	15.7	9.98	64.87 ± 1.48	0.223 ± 0.049	0.035	7.1	34.39
BGPS 3442	73.09 ± 2.76	0.180 ± 0.035	0.023	13.5	10.63	77.31 ± 2.49	0.374 ± 0.075	0.026	13.7	59.83
BGPS 3604	48.00 ± 0.42	0.704 ± 0.061	0.070	23.6	138.3	46.26 ± 0.92	0.314 ± 0.059	0.041	10.5	146.34
BGPS 3627	79.61 ± 3.54	0.608 ± 0.148	0.033	27.8	20.63	80.16 ± 2.28	0.454 ± 0.125	0.041	13.8	41.80
BGPS 3656	36.05 ± 2.38	0.219 ± 0.066	0.074	5.1	10.15	–	–	–	–	
BGPS 3686	77.99 ± 0.61	0.275 ± 0.041	0.041	13.7	4.05	80.55 ± 1.67	0.454 ± 0.079	0.033	20.5	21.30
BGPS 3710	74.47 ± 0.46	0.258 ± 0.054	0.049	19.2	1.56	73.60 ± 1.09	0.238 ± 0.053	0.033	13.7	6.38
BGPS 3822	56.49 ± 5.06	0.576 ± 0.106	0.016	55.1	12.48	50.09 ± 2.49	0.526 ± 0.084	0.029	23.8	35.04
BGPS 3982	53.85 ± 0.31	0.298 ± 0.026	0.070	7.7	80.58	54.14 ± 0.58	0.556 ± 0.056	0.064	12.0	316.89
BGPS 4029	81.45 ± 1.01	0.435 ± 0.048	0.039	22.5	10.36	82.68 ± 0.75	0.936 ± 0.081	0.074	21.3	47.90
BGPS 4082	99.33 ± 1.05	0.310 ± 0.045	0.035	16.9	18.38	98.64 ± 0.36	0.640 ± 0.059	0.100	11.0	93.33
BGPS 4230	108.83 ± 2.92	0.680 ± 0.170	0.029	41.4	30.20	–	–	–	–	–
BGPS 4294	56.10 ± 0.29	0.111 ± 0.021	0.058	3.6	7.54	55.88 ± 0.27	0.171 ± 0.029	0.068	4.3	24.11
BGPS 4297	–	–	–	–	–	56.01 ± 0.50	0.295 ± 0.038	0.058	6.9	43.88
BGPS 4356	110.81 ± 0.46	0.338 ± 0.038	0.064	9.4	12.76	111.31 ± 0.87	0.205 ± 0.053	0.039	6.8	16.86
BGPS 4375	–	–	–	–	–	91.66 ± 0.40	0.185 ± 0.033	0.061	5.1	11.55
BGPS 4396	110.04 ± 1.30	0.155 ± 0.048	0.029	8.6	6.64	107.46 ± 1.67	0.414 ± 0.079	0.035	13.5	44.49
BGPS 4402	101.44 ± 0.73	0.279 ± 0.043	0.041	12.2	8.60	99.33 ± 1.03	0.404 ± 0.071	0.051	10.4	48.51
BGPS 4472	47.04 ± 0.88	0.501 ± 0.075	0.051	19.1	9.28	49.12 ± 0.89	1.071 ± 0.108	0.086	20.7	76.84
BGPS 5021	80.08 ± 0.30	0.274 ± 0.038	0.078	7.8	13.11	79.65 ± 0.21	0.731 ± 0.063	0.135	12.0	68.09
BGPS 5064	99.81 ± 0.42	0.425 ± 0.061	0.074	15.6	17.23	100.07 ± 0.90	0.541 ± 0.049	0.061	14.7	75.41
BGPS 5114	65.63 ± 0.26	0.420 ± 0.038	0.093	11.3	9.66	64.93 ± 0.25	0.598 ± 0.053	0.138	8.6	30.46
BGPS 5243	96.79 ± 0.21	0.146 ± 0.024	0.068	4.3	6.10	96.93 ± 0.25	0.270 ± 0.040	0.070	6.0	32.04

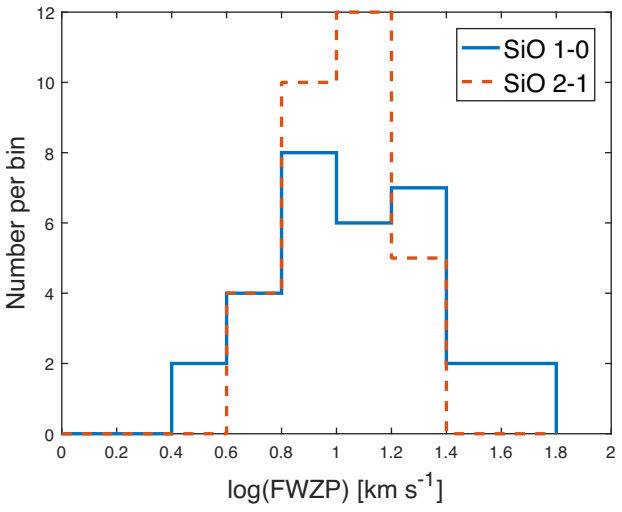

Figure 2. The histogram of the line widths (FWZP) of the SiO 1–0 and 2–1 lines.

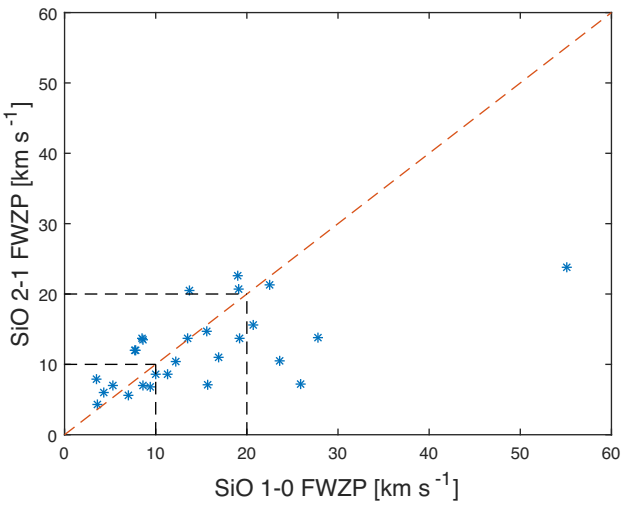

Figure 3. The comparison of the FWZPs of the SiO 1–0 and 2–1 lines of corresponding sources. The dashed line indicates the position where the FWZPs of the SiO lines are equal.

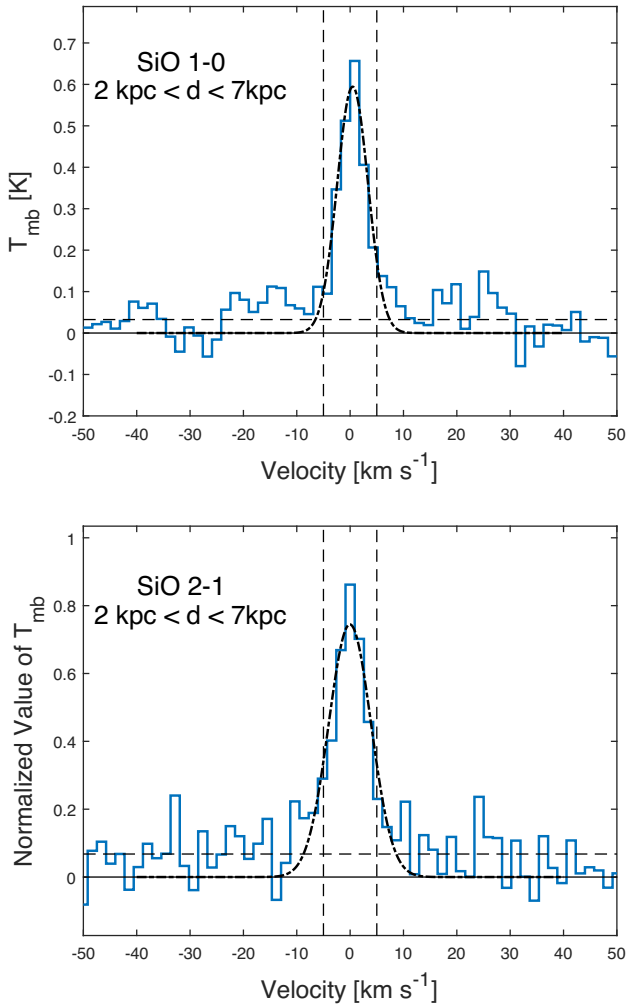

Figure 4. The distance-weighted average SiO line profiles of the detected sources located between 2–7 kpc. The vertical and horizontal dashed lines indicate the velocity range from –5 to 5 km s^{-1} and the rms noise levels. The Gaussin fittings to the profiles are plotted as dash–dotted lines.

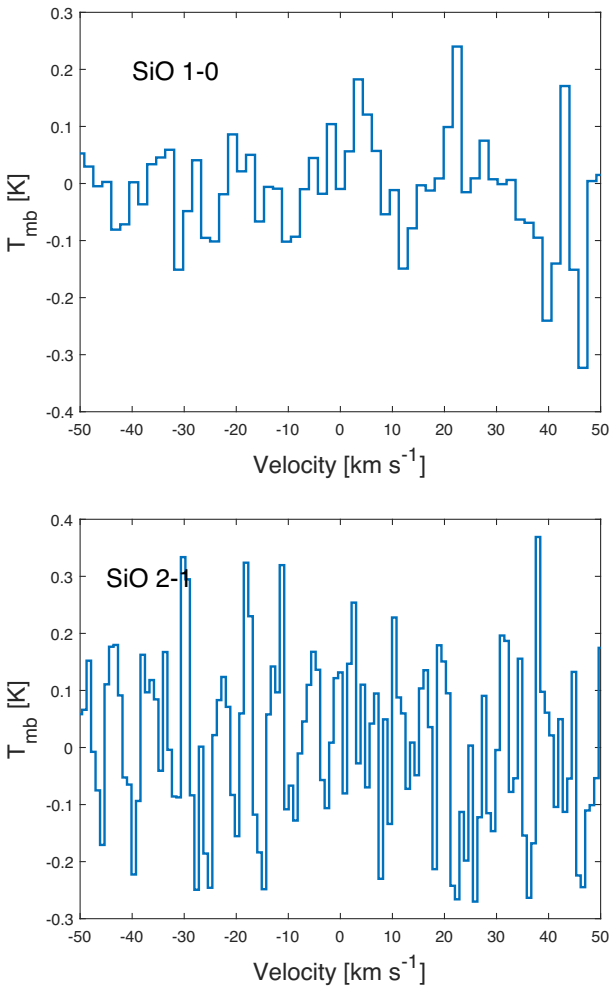

Figure 5. The distance-weighted average profiles of the SiO 1–0 and 2–1 lines for the targets without clear detections.

be different. The excitation temperature of the shocked gas emitting the SiO lines is unclear, but $T_{\rm ex}$ = 10K is considered as a good assumption of excitation temperature for the physical properties of SCCs by previous studies (Leurini et al. 2014; Csengeri et al. 2016). Csengeri et al. (2016) also pointed out that the estimated column density of the SiO molecules does not vary significantly with a appropriate excitation temperature ranging from 5 to 30 K. The estimated SiO column densities are written in Table 5. The estimated SiO column densities derived from the observed fluxes of the SiO 1–0 line and the SiO 2–1 line range from 5.99×10^{11} to 4.32×10^{12} cm^{-2} and from 3.07×10^{11} to 2.32×10^{12} cm^{-2}, respectively. The median values are 1.83×10^{12} and 8.75×10^{11} cm^{-2}, and the mean values are 2.16×10^{12} and 9.92×10^{11} cm^{-2}. The range of the estimated SiO column densities is not significantly different from the results for the starless clumps in the previous works (Csengeri et al. 2016; Li et al. 2019). In most sources, the SiO column densities estimated from the SiO 1–0 and 2–1 lines cannot match even if the $T_{\rm ex}$ is changed in a range of 5–100 K. What causes the difference between the estimated values derived from the SiO 1–0 and 2–1 lines is discussed in Section 4.1.

In order to estimate the SiO abundance, the column density of H_2 should be also calculated. The 1.1-mm continuum thermal dust emission from BGPS is used to estimate the gas mass and column density of the SCCs (Ginsburg et al. 2013) through the formula (Li et al. 2019) below

$$M_{\rm gas} = \eta \frac{S_\nu d^2}{B_\nu(T)\kappa_\nu} \tag{2}$$

and

$$N({\rm H_2}) = \frac{\eta F_\nu}{B_\nu(T)\Omega\kappa_\nu\mu_{H_2}m_{\rm H}} \quad , \tag{3}$$

where $M_{\rm gas}$ is the clump mass, η = 100 is the gas-to-dust mass ratio (Schuller et al. 2008), S_ν is the integrated continuum flux at the frequency of ν, d is the source distance given in Calahan et al. (2018), $B_\nu(T)$ is the intensity of a blackbody at the temperature T and frequency ν, and $\kappa_\nu = 10[\nu/(1.2 \times 10^{12})]^{1.5}$ cm^2 g^{-1} is the dust opacity (Hildebrand 1983). $N(H_2)$ is the column density of H_2, F_ν is the flux density, and Ω is the beam solid angle. $\mu_{H_2} = 2.8$ is the molecular weight of a hydrogen molecule (Kauffmann et al. 2008) and m_H is the mass of a hydrogen atom. The gas mass $M_{\rm gas}$ is derived from the total 1.1-mm continuum flux towards an SCC, but the H_2 column density is calculated by using the continuum flux with a beam size of 40 arcsec. Assuming that the dust temperature is equal

Table 4. The properties of the SiO 3–2 line emitted from corresponding sources. L_{SiO3-2} is the luminosity.

Name	V_{lsr} (km s^{-1})	$\int T_{mb} dv$ (K km s^{-1})	T_{mb} (K)	FWZP (km s^{-1})	L_{SiO3-2} ($10^{-7} L_{\odot}$)
BGPS 3110	17.92 ± 0.14	0.588 ± 0.035	0.148	6.8	15.85
BGPS 3114	22.20 ± 0.31	0.400 ± 0.081	0.148	3.5	8.75
BGPS 3118	19.77 ± 1.66	0.573 ± 0.138	0.166	9.2	19.46
BGPS 3686	80.79 ± 1.18	0.454 ± 0.085	0.041	13.8	26.89
BGPS 4472	50.94 ± 0.66	1.300 ± 0.118	0.103	16.1	94.59
BGPS 5064	101.30 ± 1.24	0.153 ± 0.043	0.029	5.6	43.26
BGPS 5114	65.47 ± 0.25	0.184 ± 0.039	0.084	3.4	14.49
BGPS 5243	97.30 ± 0.57	0.261 ± 0.059	0.049	9.3	30.11

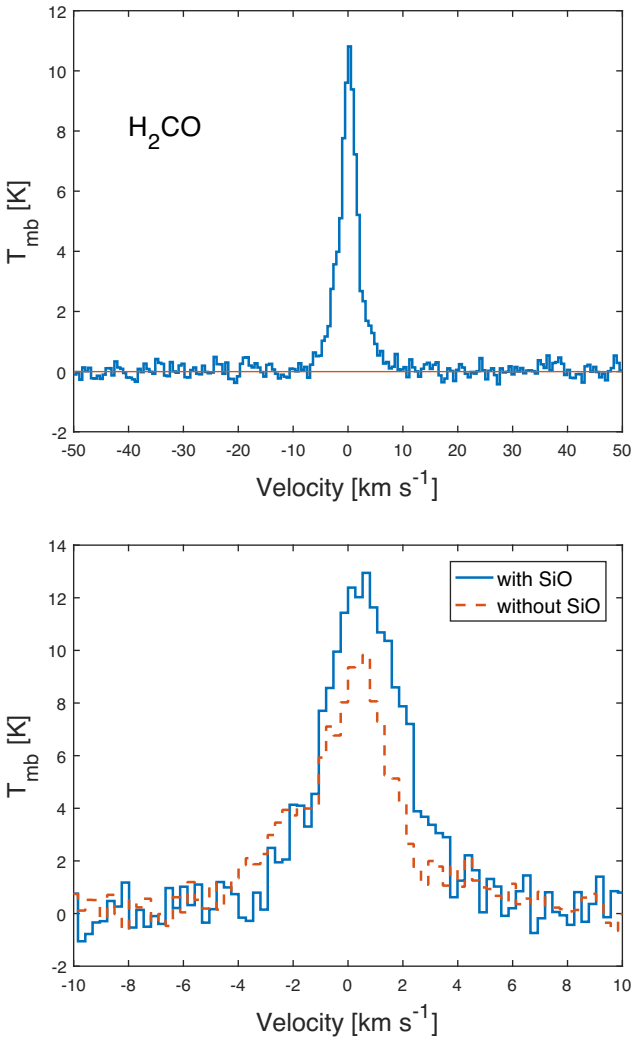

Figure 6. The distance-weighted average line profile of H_2CO emissions is presented in the top panel. The comparison between the distance-weighted average H_2CO line profiles from the sources with and without SiO emissions is displayed in the lower panel.

to the NH_3 derived gas kinetic temperature provided by Svoboda et al. (2016), the estimated gas masses and H_2 column densities of the SCCs which exhibit SiO emission are listed in Table 5. The mass distribution of the SCCs is showed in Fig. 7. The mass distributions of the sources with and without SiO emission are also showed in Fig. 7. The mean and median gas masses of the total SCC sample are 697.1 and 372.2 $M_{\odot}$, respectively. And the mean masses of the SCCs with and without SiO emission are 937.3 and 620.6 $M_{\odot}$. The median masses of the SCCs with and without SiO emission are 535.5 and 243.4 $M_{\odot}$. By using Kolmogorov–Smirnov test, it is found that the mass distributions of the two samples are not significantly different.

After the column densities of SiO and H_2 molecules are calculated, the SiO abundances are obtained and also presented in Table 5. In the SCCs, the H_2 column density ranges from 1.14×10^{21} to 5.89×10^{22} cm^{-2}, and the mean and median values are 6.18×10^{21} and 4.84×10^{21} cm^{-2}, respectively. The SiO abundance estimated from the SiO 1–0 line ranges from 3.70×10^{-11} to 1.09×10^{-9}, and the average and median values are 3.36×10^{-10} and 2.77×10^{-10}, respectively. Correspondingly, the SiO abundance derived from the properties of the SiO 2–1 line ranges from 2.02×10^{-11} to 4.03×10^{-10}. In addition, the mean and median values are 1.59×10^{-10} and 1.41×10^{-10}, respectively.

3.5 H_2CO column density and abundance

The column density of the H_2CO molecules is also calculated through equation (1) under the same assumptions but with corresponding parameters for H_2CO molecules. The excitation temperature is assumed to be the NH_3 derived gas kinetic temperature. The derived column densities are provided in Table 1 and they range from 1.03×10^{12} to 1.16×10^{14} cm^{-2}. The average column density is 1.27×10^{13} cm^{-2} and the median value is 7.94×10^{12} cm^{-2}. The H_2CO abundances estimated by comparing column densities of H_2 and H_2CO molecules are also written in Table 1. The abundances range from 1.77×10^{-10} to 1.96×10^{-8}. The average and median values are 2.57×10^{-9} and 1.45×10^{-9}, respectively. The estimated values of the H_2CO abundances are similar to those provided in previous works (Vichietti et al. 2016).

3.6 The uncertainties of the estimation for gas mass and molecular hydrogen column density

According to the BGPS v2.1 data provided by Ginsburg et al. (2013), the average 1σ uncertainty of the 1.1-mm continuum flux density with a beam size of 40 arcsec is 34.69 per cent, and the maximum uncertainty is 81.48 per cent. The average uncertainty of the 1.1-mm continuum integrated flux density is 20.14 per cent and the maximum value is 46.04 per cent. The NH_3 derived gas kinetic temperature is used to estimate the gas masses and column densities. For most sources, the uncertainty of the gas kinetic temperature is lower than 3 per cent. The uncertainties of the gas-to-dust ratio η and the dust opacity κ_{ν} are assumed to be 23 and 28 per cent as in Li et al. (2019), respectively. Then the uncertainties of gas mass and H_2 column

Table 5. The column densities and abundances of the SiO molecules estimated from the flux densities of the SiO 1–0, 2–1, and 3–2 lines and the excitation temperature is assumed to be 10 K.

Name	M ($M_\odot$)	$N(H_2)$ (cm^{-2})	SiO 1–0		SiO 2–1		SiO 3–2	
			N(SiO) (cm^{-2})	X(SiO)	N(SiO) (cm^{-2})	X(SiO)	N(SiO) (cm^{-2})	X(SiO)
BGPS 2724	18.5	2.77×10^{21}	5.99×10^{11}	2.16×10^{-10}	5.27×10^{11}	1.90×10^{-10}	–	–
BGPS 2945	52.9	6.03×10^{21}	1.24×10^{12}	2.05×10^{-10}	–	–	–	–
BGPS 2970	597.6	1.00×10^{22}	4.23×10^{12}	4.23×10^{-10}	7.01×10^{11}	7.01×10^{-11}	–	–
BGPS 2976	36.6	4.34×10^{21}	2.58×10^{12}	5.94×10^{-10}	8.75×10^{11}	2.02×10^{-10}	–	–
BGPS 3110	370.8	1.72×10^{22}	3.71×10^{12}	2.16×10^{-10}	2.03×10^{12}	1.18×10^{-10}	1.01×10^{12}	5.87×10^{-11}
BGPS 3114	5371.3	5.89×10^{22}	2.18×10^{12}	3.71×10^{-11}	1.19×10^{12}	2.02×10^{-11}	6.85×10^{11}	1.16×10^{-11}
BGPS 3118	365.4	9.36×10^{21}	2.64×10^{12}	2.82×10^{-10}	1.44×10^{12}	1.54×10^{-10}	9.83×10^{11}	1.05×10^{-10}
BGPS 3128	695.2	8.79×10^{21}	1.65×10^{12}	1.87×10^{-10}	8.75×10^{11}	9.96×10^{-11}	–	–
BGPS 3139	1417.0	7.75×10^{21}	1.00×10^{12}	1.29×10^{-10}	3.07×10^{11}	3.96×10^{-11}	–	–
BGPS 3220	415.4	9.80×10^{21}	1.26×10^{12}	1.29×10^{-10}	7.47×10^{11}	7.65×10^{-11}	–	–
BGPS 3247	380.6	4.18×10^{21}	–	–	1.21×10^{12}	2.89×10^{-10}	–	–
BGPS 3344	1776.1	4.96×10^{21}	1.58×10^{12}	3.20×10^{-10}	4.83×10^{11}	9.73×10^{-11}	–	–
BGPS 3442	254.3	5.15×10^{21}	1.11×10^{12}	2.15×10^{-10}	8.11×10^{11}	1.58×10^{-10}	–	–
BGPS 3604	2676.0	5.61×10^{21}	4.32×10^{12}	7.69×10^{-10}	6.84×10^{11}	1.22×10^{-10}	–	–
BGPS 3627	766.4	3.41×10^{21}	3.73×10^{12}	1.10×10^{-9}	9.85×10^{11}	2.89×10^{-10}	–	–
BGPS 3656	161.4	3.58×10^{21}	1.35×10^{12}	3.77×10^{-10}	–	–	–	–
BGPS 3686	404.7	6.01×10^{21}	1.69×10^{12}	2.82×10^{-10}	9.85×10^{11}	1.64×10^{-10}	7.76×10^{11}	1.29×10^{-10}
BGPS 3710	133.4	6.22×10^{21}	1.58×10^{12}	2.55×10^{-10}	5.16×10^{11}	8.28×10^{-11}	–	–
BGPS 3822	392.8	9.00×10^{21}	3.54×10^{12}	3.93×10^{-10}	1.15×10^{12}	1.27×10^{-10}	–	–
BGPS 3982	2177.2	3.39×10^{21}	1.83×10^{12}	5.39×10^{-10}	1.21×10^{12}	3.57×10^{-10}	–	–
BGPS 4029	473.4	9.65×10^{21}	2.67×10^{12}	2.77×10^{-10}	2.03×10^{12}	2.11×10^{-10}	–	–
BGPS 4082	336.3	5.10×10^{21}	1.91×10^{12}	3.74×10^{-10}	1.39×10^{12}	2.73×10^{-10}	–	–
BGPS 4230	623.2	7.67×10^{21}	4.18×10^{12}	5.43×10^{-10}	–	–	–	–
BGPS 4294	613.0	4.39×10^{21}	6.86×10^{11}	1.56×10^{-10}	3.73×10^{11}	8.52×10^{-11}	–	–
BGPS 4297	142.8	2.96×10^{21}	–	–	6.43×10^{11}	2.17×10^{-10}	–	–
BGPS 4356	1727.4	1.02×10^{22}	2.07×10^{12}	2.03×10^{-10}	4.46×10^{11}	4.37×10^{-11}	–	–
BGPS 4375	117.5	4.54×10^{21}	–	–	4.02×10^{11}	8.86×10^{-11}	–	–
BGPS 4396	808.3	1.11×10^{22}	9.58×10^{11}	8.61×10^{-11}	8.98×10^{11}	8.11×10^{-11}	–	–
BGPS 4402	253.0	6.23×10^{21}	1.72×10^{12}	2.76×10^{-10}	8.75×10^{11}	1.40×10^{-10}	–	–
BGPS 4472	130.3	5.76×10^{21}	3.08×10^{12}	5.34×10^{-10}	2.32×10^{12}	4.03×10^{-10}	2.23×10^{12}	3.87×10^{-10}
BGPS 5021	832.0	8.51×10^{21}	1.68×10^{12}	1.98×10^{-10}	1.59×10^{12}	1.87×10^{-10}	–	–
BGPS 5064	1958.2	4.77×10^{21}	2.62×10^{12}	5.48×10^{-10}	1.18×10^{12}	2.47×10^{-10}	2.61×10^{11}	5.48×10^{-11}
BGPS 5114	821.9	7.02×10^{21}	2.58×10^{12}	3.67×10^{-10}	1.30×10^{12}	1.85×10^{-10}	3.14×10^{11}	4.48×10^{-11}
BGPS 5243	421.9	4.75×10^{21}	8.98×10^{11}	1.89×10^{-10}	5.85×10^{11}	1.23×10^{-10}	4.48×10^{11}	9.41×10^{-11}

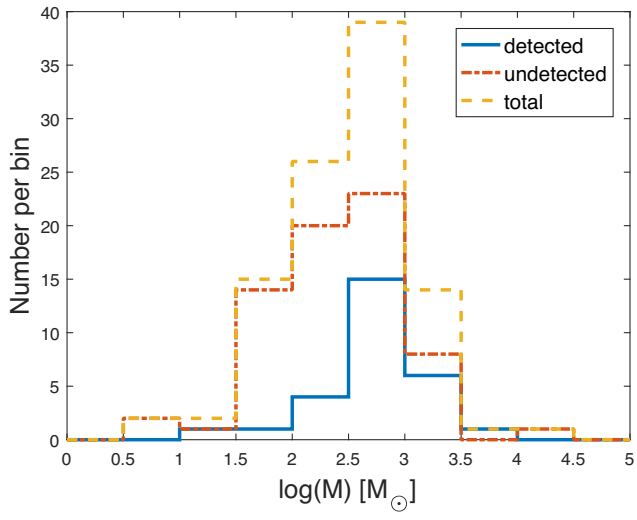

Figure 7. The mass distributions of the sources. The solid line represents the mass distribution of the sources with SiO emission. The dash–dotted line shows the mass distribution of the sources without SiO emission. And the dashed line display the mass distribution of all the sources.

density for the SCCs are ∼ 44 and ∼ 53 per cent, respectively. When analysing some trends about the gas masses and column densities among the SCCs, these uncertainties are not important because of the large ranges of gas masses and H_2 column densities among the SCCs. And the estimated molecular abundances calculated from H_2 column densities are still meaningful since very accurate values of the abundances are not indispensable.

4 DISCUSSIONS

4.1 The excitation condition of the shocked gas

From Table 5, it is showed that the SiO column densities estimated from the SiO 1–0 and 2–1 lines are different. And in Fig. 8, it is obvious that the estimated column densities from the SiO 1–0 line are higher than those from the SiO 2–1 line in almost all of the sources with two line detections. Generally, the beam-filling factor and the non-LTE condition could make this difference. Since the SiO column density estimated from the SiO 1–0 line is higher, the beam-filling factor of the SiO 1–0 line would be higher if this was the main cause. Considering the region covered by the SiO 2–1 observation is also covered by the SiO 1–0 observation, the outer region only covered by the SiO 1–0 observation must be denser than those in the centre region if the beam-filling factor of the SiO 1–0 line is

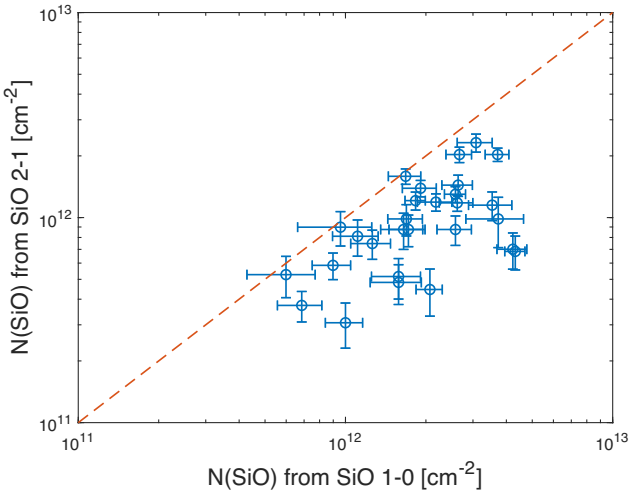

Figure 8. The comparison between the SiO column densities estimated from the SiO 1–0 and 2–1 lines of the sources both detected in the two SiO lines. The estimates are calculated under the LTE assumption. The dashed line represents the position where the two estimated column densities are equal.

higher. This may be true in several sources, but cannot be true in most SCCs with detected SiO 2–1 emission because the pointing position should not always be very far from the shocked gas. So the beam-filling factor and observational coverage should not be the main cause. Then, the lower estimated column densities from the SiO 2–1 line are probably attributed to the non-LTE condition due to low density of H_2 molecules. Commonly, the SiO column densities estimated by using the line fluxes of low SiO rotational transitions tend to be overestimated if the calculation is treated with the LTE assumption that is not satisfied in fact. Therefore, we suggest that the SiO column densities from the SiO 1–0 line could be overestimated because of the non-LTE condition if the beam dilution effect is not important. In order to check this suggestion, we perform the non-LTE analysis by using RADEX (van der Tak et al. 2007) with a plane-parallel slab geometry to estimate the SiO column densities under the assumption of the beam-filling factors of unity. The resulting SiO column densities are lower than those estimated from the SiO 1–0 line under the LTE assumption in almost all the sources. Although these non-LTE estimates are not necessarily more accurate than the LTE values due to the unknown beam-filling factors, the analysis still supports a non-LTE environment of the SiO molecules.

4.2 The fraction of the shocked gas in SCCs

The comparison between the distance-weighted average H_2CO line profiles from the sources associated with and without SiO emission is plotted in the lower panel of Fig. 6. There is no essential difference in these two line profiles. The corresponding average line areas are 15.00 and 12.08 K km s^{-1} for the sources with and without SiO emission, respectively. The average line area for the sources associated with SiO emission is higher, but the difference between these two average values is not statistically significant at the 5 per cent significance level.

The luminosities of the SiO and H_2CO lines as a function of the SCC mass are showed in Fig. 9. The sample is distance limited and only includes the sources located between 3–7 kpc. The spearman test is used to evaluate the correlation between the H_2CO line luminosity

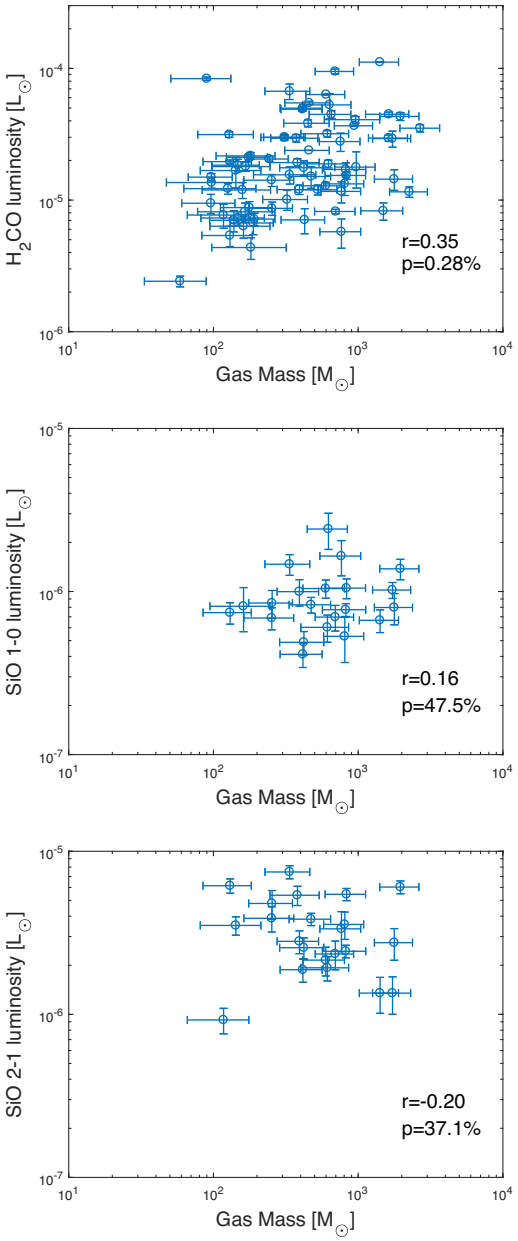

Figure 9. The luminosity of the H_2CO and SiO lines as a function of the gas mass of the SCCs. The distance limited sample includes the detected sources located between 3–7 kpc.

and the gas mass. The Spearman's rank correlation coefficient is 0.35 and the *p*-value is 0.28 per cent. So the positive correlation between the H_2CO line luminosity and the clump mass is statistically significant. The correlation can also be found from the top panel of Fig. 9. This result is not strange since H_2CO molecules are regarded as a good tracer of dense gas of molecular cloud (Guo et al. 2016). On the contrary, the luminosity of the SiO lines is not significantly correlated to the clump mass in the spearman test. The coefficients of the correlation between the luminosities of the SiO 1–0 and 2–1 lines and the clump mass are 0.16 and −0.20, and the corresponding *p*-values are 47.5 and 37.1 per cent, respectively. This implies that the relation between the shocks and the clump mass is not obvious.

4.3 The origin of the shocks in SCCs

The SCCs can be representative of the very early stage of star formation. In dense clouds, SiO is the best tracer to probe the shocks and is very useful to evaluate the level of star-forming activities. According to our observations of the SiO lines, shocks seem to be quite common even in the early evolutionary age of star formation. The broad SiO line profiles (FWZP $> 20\,\mathrm{km\,s^{-1}}$) are obtained in 10 sources. They are probably associated with fast shocks due to protostellar outflows (Martín-Pintado, Bachiler & Fuente 1992; Jiménez-Serra et al. 2010). For the distance-weight average SiO 1–0 and 2–1 spectra presented in Fig. 4, the fitted Gaussian curve to the SiO 1–0 spectrum has relatively narrow line width with a FWHM of $6.8\,\mathrm{km\,s^{-1}}$, but the high-velocity wings are obvious. Moreover, the fitted curve to the SiO 2–1 spectrum with a $9.4\,\mathrm{km\,s^{-1}}$ FWHM can be classified as a broad component in Csengeri et al. (2016). These results suggest some Class 0-like protostars deeply embedded in these SCCs; and SiO line emission seems to be a more powerful tool to detect deeply embedded protostars and their driving shocks than infrared emission (Csengeri et al. 2016). In this work, the signal-to-noise ratios of the detected SiO line profiles are mostly not high ($\int T_{\mathrm{mb}}\mathrm{d}v < 10\sigma_{\mathrm{area}}$). Considering the limiting sensitivity of the observations that make the SiO line widths possibly underestimated, there must be more sources hosting protostars. The other sources show relatively narrower line widths (FWZP $< 20\,\mathrm{km\,s^{-1}}$). About the formation of the narrow velocity component, several explanations are provided. One is low-velocity shocks due to large scale cloud–cloud collisions (Jiménez-Serra et al. 2010; Louvet et al. 2016), and another is less powerful outflows from intermediate and low-mass protostars (Beuther & Sridharan 2007; Inoue & Fukui 2013; Sanhueza et al. 2013). So far, the origin of the shocks in SCCs cannot be solved because of the single-dish observations in the current works.

5 SUMMARY

In this paper, we used the KVN 21-m radio telescopes to perform the single-point observations of the SiO 1–0, 2–1, and 3–2 lines and the H_2CO $2_{12}-1_{11}$ line towards 100 SCCs. The sample of SCCs is provided by Calahan et al. (2018) and was identified from the BGPS v2.1 catalogue (Ginsburg et al. 2013). The detection rates of the four lines are 31.0, 31.0, 19.5, and 93.0 per cent, respectively. Since SiO is a tracer of shocks, the detection rates of the SiO lines suggest that shocks are quite common in the SCCs as very early stage of star formation. The SiO-detected sources provide a sample of targets for further studies of the origin of shocks in SCCs using high angular resolution observations. The details of our results are summarized as follows:

1. According to the FWZP velocity ranges of the detected SiO lines, a significant fraction ($\sim$ 29.4 per cent) of the SiO spectra have broad line widths (FWZP $> 20\,\mathrm{km\,s^{-1}}$). These broad line widths are regarded as indicators of the fast shocks due to outflows from high-mass protostars. The sources with fast shocks should be not real starless but protostellar clumps. In addition, about 40 per cent of the SiO detections have narrow line widths (FWZP $< 10\,\mathrm{km\,s^{-1}}$) possibly associated with low-velocity shocks. This result implies that slow shocks are not rare in the early stage of star formation. The origins of the shocks marked by the SiO emissions in the SCCs need to be studied by further high-resolution mapping observations.
2. The H_2CO line widths are $\sim 3.0\,\mathrm{km\,s^{-1}}$ and relatively much narrower than those of the SiO lines . This indicates the locations of SiO (shocked gas) and the H_2CO molecules are different.
3. The estimated SiO column densities in the SCCs are $\sim 10^{12}\,\mathrm{cm^{-2}}$ under the LTE assumption. By comparing the estimated values derived from the SiO 1–0 and 2–1 line fluxes, the SiO molecules are found to be non-LTE; and the estimated values from the line fluxes of low transitions should be overestimated without the consideration about beam dilution effect. The estimated SiO abundances measured against H_2 range from 2.02×10^{-11} to 1.09×10^{-9} and they should be also overestimated. On the other hand, the estimated column densities and abundances could be underestimated due to a beam dilution.
4. The estimated H_2CO column densities in the SCCs range from 1.03×10^{12} to $1.16 \times 10^{14}\,\mathrm{cm^{-2}}$. The median column density is $7.94 \times 10^{12}\,\mathrm{cm^{-2}}$. The estimated H_2CO abundances are from 1.77×10^{-10} to 1.96×10^{-8}, and the median value is 1.45×10^{-9}.
5. The positive correlation of the observed luminosity of the H_2CO line and the gas mass of the SCCs is obvious. On the other hand, the SiO line luminosities seem to be not significantly correlated to the gas mass. This result also implies that the clump mass is not a direct cause of the shocks formed in the early stage of star formation.

ACKNOWLEDGEMENTS

We are grateful to all staff members in Korean VLBI Network (KVN) who helped to operate the array and to correlate the data. The KVN is a facility operated by Korea Astronomy and Space Science Institute (KASI). This work is supported by funding from National Key Basic Research and Development Program of China (grant No. 2017YFA0402604), National Science Foundation of China grant no. 11590783, U1731237, and China Postdoctoral Science Foundation grant no. 2020M671267.

DATA AVAILABILITY STATEMENT

The data underlying this paper will be shared on reasonable request to the corresponding author.

REFERENCES

Beuther H., Sridharan T. K., 2007, ApJ, 668, 348
Calahan J. K. et al., 2018, ApJ, 862, 63
Cosentino G. et al., 2018, MNRAS, 474, 3760
Csengeri T. et al., 2016, A&A, 586, A149
Duarte-Cabral A., Bonetmps S., Motte F., Gusdorf A., Csengeri T., Schneider N., Louvet F., 2014, A&A, 570, A1
Ellsworth-Bowers T. P., Rosolowsky E., Glenn J., Ginsburg A., Evnas N. J., II, 2015, ApJ, 799, 29
Ginsburg A. et al., 2013, ApJS, 208, 14
Guo W.-H. et al., 2016, Astrophys Space Sci, 361, 264
Gusdorf A., Pineau Des Forêts G., Cabrit S., Flower D. R., 2008, A&A, 490, 695
Hildebrand R. H., 1983, QJRAS, 24, 267
Inoue T., Fukui Y., 2013, ApJ, 774, 31
Jiménez-Serra I., Caselli P., Tan J. C., Hernandez A. K., Fontani F., Butler M. J., van Loo S., 2010, MNRAS, 406, 187
Kauffmann J., Bertoldi F., Bourke T. L., Evans N. J., II, Lee C. W., 2008, A&A, 487, 993
Kim K.-T. et al., 2011, JKAS, 44, 81
Leurini S., Codella C., López-Sepulcre A., Gusdorf A., Csengeri T., Anderl S., 2014, A&A, 570, A49
Li S.-H. et al., 2019, ApJ, 878, 29
Louvet F. et al., 2016, A&A, 595, A122
Mangum J. G., Shirley Y. L., 2015, PASP, 127, 266
Martín-Pintado J., Bachiler R., Fuente A., 1992, A&A, 254, 315
Matzner C. D., 2017, preprint (arXiv:1712.01457)

Motte F., Bontemps S., Louvet F., 2018, ARA&A, 56, 41
Nguyen Luong Q. et al., 2011, A&A, 529, A41
Nguyen Luong Q. et al., 2013, ApJ, 775, 88
Nishimura Y., Watanabe Y., Harada N., Kohno K., Yamamoto S., 2019, ApJ, 879, 65
Sanhueza P., Jackson J. M., Foster J. B., Jimenez-Serra I., Dirienzo W. J., Pillai T., 2013, ApJ, 773, 123
Schuller F. et al., 2009, A&A, 504, 415
Svoboda B. E. et al., 2016, ApJ, 822, 59
Svoboda B. E. et al., 2019, ApJ, 886, 36
Tang X. D. et al., 2017, A&A, 600, A16
Traficante A., Fuller G. A., Peretto N., Pineda J. E., Molinari S., 2015, MNRAS, 451, 3089
Urquhart J. S. et al., 2018, MNRAS, 473, 1059
van der Tak F. F. S., van Dishoeck E. F., Evans N. J., II, Blake G. A., 2000, ApJ, 537, 283
van der Tak F. F. S., Black J. H., Schöier F. L., Jansen D. J., van Dishoeck E. F., 2007, A&A, 468, 627
Vichietti R. M., Spada R. F. K., da Silva A. B. F., Machado F. B. C., Haiduke R. L., 2016, ApJS, 225, 2

APPENDIX: THE NOISE LEVELS AND THE SIO SPECTRA FOR INDIVIDUAL SOURCES

In this work, the integration times and weather conditions of the observations towards individual sources are different. In order to assess this effect on the detection rates of the SiO lines, the rms noise at the velocity resolution of 1 km s^{-1} in the SiO and H_2CO lines of the observed sources are calculated and listed in Table A1. The noise distributions are presented in Fig. A1. The median noise levels of the entire sample and the sources with SiO detections are plotted, respectively. The differences between these two kinds of median values are not very significant. So the detection rates are still meaningful. The spectra of the detected SiO lines for individual sources are provided in Fig. A2.

Table A1. The noise levels at the velocity resolution of 1 km s^{-1} in the H_2CO and SiO 1–0, 2–1, and 3–2 spectra for individual sources are written. Which instruments used in observations are also presented. YS, US, and TN mean Yonsei, Ulsan and Tamna telescopes, respectively.

Name	Telescope	$\delta T_{mb}(H_2CO)$ [K]	δT_{mb}(SiO(1–0)) [K]	δT_{mb}(SiO(2–1)) [K]	δT_{mb}(SiO(3–2)) [K]
BGPS 2427	YS	0.064	0.017	0.027	0.018
BGPS 2430	US	0.053	0.026	0.030	0.031
BGPS 2432	TN	0.031	0.025	0.025	0.017
BGPS 2437	YS	0.064	0.021	0.024	0.018
BGPS 2533	US	0.061	0.024	0.032	0.025
BGPS 2564	TN	0.025	0.017	0.015	0.022
BGPS 2693	US	0.061	0.035	0.034	–
BGPS 2710	YS	0.056	0.023	0.024	0.015
BGPS 2724	US	0.081	0.020	0.023	0.022
BGPS 2732	TN	0.028	0.023	0.018	–
BGPS 2742	US	0.083	0.020	0.016	0.019
BGPS 2762	YS + US	0.064	0.027	0.023	0.018
BGPS 2931	TN + US	0.059	0.029	0.023	0.019
BGPS 2940	YS	0.026	0.021	0.032	–
BGPS 2945	YS	0.026	0.013	0.022	–
BGPS 2949	YS	0.028	0.021	0.034	–
BGPS 2970	YS	0.033	0.015	0.024	0.056
BGPS 2971	US	0.075	0.015	0.014	0.014
BGPS 2976	TN	0.022	0.013	0.014	0.019
BGPS 2984	TN	0.025	0.031	0.025	0.019
BGPS 2986	US	0.064	0.039	0.027	0.031
BGPS 3018	TN	0.031	0.033	0.025	–
BGPS 3030	TN	0.025	0.015	0.016	0.014
BGPS 3110	US	0.067	0.022	0.016	0.014
BGPS 3114	US	0.017	0.013	0.018	0.044
BGPS 3117	US	0.019	0.035	0.027	–
BGPS 3118	YS	0.033	0.013	0.020	0.044
BGPS 3125	YS	0.031	0.023	0.042	–
BGPS 3128	YS	0.131	0.015	0.029	–
BGPS 3129	TN	0.047	0.027	0.021	0.014
BGPS 3134	TN	0.014	0.017	0.021	–
BGPS 3139	TN	0.014	0.015	0.014	–
BGPS 3151	TN	0.017	0.035	0.034	–
BGPS 3220	YS	0.033	0.015	0.022	–
BGPS 3243	US	0.042	0.041	0.046	–
BGPS 3247	US	0.042	0.033	0.036	–
BGPS 3276	US	0.042	0.050	0.046	–
BGPS 3300	TN	0.050	0.025	0.023	–
BGPS 3302	TN	0.036	0.042	0.052	–

Table A1 *– continued*

Name	Telescope	$\delta T_{\rm mb}(H_2CO)$ [K]	$\delta T_{\rm mb}$(SiO(1–0)) [K]	$\delta T_{\rm mb}$(SiO(2–1)) [K]	$\delta T_{\rm mb}$(SiO(3–2)) [K]
BGPS 3306	TN	0.042	0.040	0.055	–
BGPS 3312	YS	0.033	0.021	0.024	–
BGPS 3315	US	0.056	0.048	0.055	–
BGPS 3344	TN	0.069	0.017	0.018	0.064
BGPS 3442	YS	0.028	0.010	0.017	–
BGPS 3444	YS	0.031	0.017	0.044	–
BGPS 3475	US	0.042	0.048	0.046	–
BGPS 3484	TN	0.058	0.052	0.061	–
BGPS 3487	YS	0.028	0.017	0.039	–
BGPS 3534	YS	0.036	0.017	0.042	–
BGPS 3604	YS	0.044	0.013	0.022	–
BGPS 3606	US	0.042	0.044	0.032	–
BGPS 3608	US	0.042	0.037	0.036	–
BGPS 3627	US	0.039	0.030	0.032	–
BGPS 3656	US	0.050	0.024	0.032	–
BGPS 3686	US	0.047	0.013	0.018	–
BGPS 3705	TN	0.036	0.029	0.039	–
BGPS 3710	TN	0.036	0.015	0.014	–
BGPS 3716	TN	0.036	0.031	0.039	–
BGPS 3736	TN	0.033	0.023	0.043	–
BGPS 3822	TN	0.050	0.015	0.018	–
BGPS 3833	YS	0.044	0.023	0.037	–
BGPS 3892	YS	0.028	0.019	0.032	–
BGPS 3922	YS	0.036	0.013	0.027	–
BGPS 3924	YS	0.033	0.019	0.039	–
BGPS 3982	YS	0.036	0.008	0.015	–
BGPS 4029	YS	0.131	0.008	0.017	–
BGPS 4082	YS	0.123	0.010	0.012	–
BGPS 4095	YS	0.105	0.010	0.017	–
BGPS 4119	TN	0.028	0.027	0.023	–
BGPS 4135	TN	0.025	0.017	0.016	–
BGPS 4140	US	0.067	0.024	0.025	–
BGPS 4145	US	0.058	0.015	0.018	–
BGPS 4191	US	0.058	0.039	0.030	–
BGPS 4230	TN	0.025	0.021	0.023	–
BGPS 4294	TN	0.025	0.013	0.014	–
BGPS 4297	YS	0.051	0.013	0.015	0.036
BGPS 4346	TN	0.025	0.027	0.025	–
BGPS 4347	TN	0.022	0.021	0.018	–
BGPS 4354	YS	0.126	0.023	0.032	–
BGPS 4356	YS	0.095	0.010	0.020	–
BGPS 4375	US	0.058	0.015	0.016	0.050
BGPS 4396	US	0.047	0.017	0.018	–
BGPS 4402	US + YS	0.031	0.015	0.021	–
BGPS 4422	YS	0.031	0.021	0.039	–
BGPS 4472	US	0.017	0.017	0.027	0.028
BGPS 4732	TN	0.042	0.029	0.027	0.017
BGPS 4827	TN	0.031	0.023	0.023	0.014
BGPS 4841	TN	0.036	0.023	0.027	0.014
BGPS 4902	TN	0.036	0.025	0.021	0.014
BGPS 4953	TN	0.036	0.029	0.023	0.017
BGPS 4962	US	0.067	0.037	0.030	0.028
BGPS 4967	YS	0.087	0.019	0.024	–
BGPS 5021	YS	0.036	0.013	0.015	–
BGPS 5064	TN	0.036	0.019	0.014	0.017
BGPS 5089	YS	0.023	0.027	0.024	0.033
BGPS 5090	YS	0.056	0.025	0.020	0.023
BGPS 5114	YS	0.077	0.010	0.017	0.021
BGPS 5166	YS	0.046	0.021	0.022	0.018
BGPS 5183	YS	0.051	0.017	0.024	0.023
BGPS 5243	YS	0.051	0.013	0.017	0.021

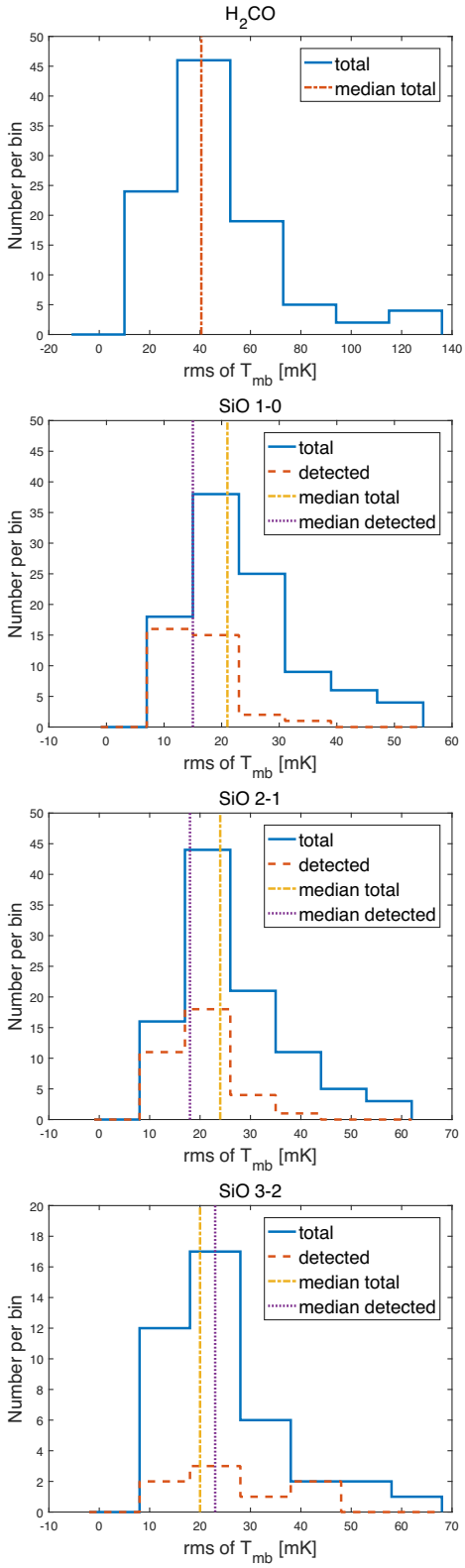

Figure A1. The noise distribution of the observations of the H_2CO and SiO lines towards the SCCs in the sample. The vertical dash–dot lines present the median noise levels for the total sample and the vertical dotted ones show the median values only for the detected sources.

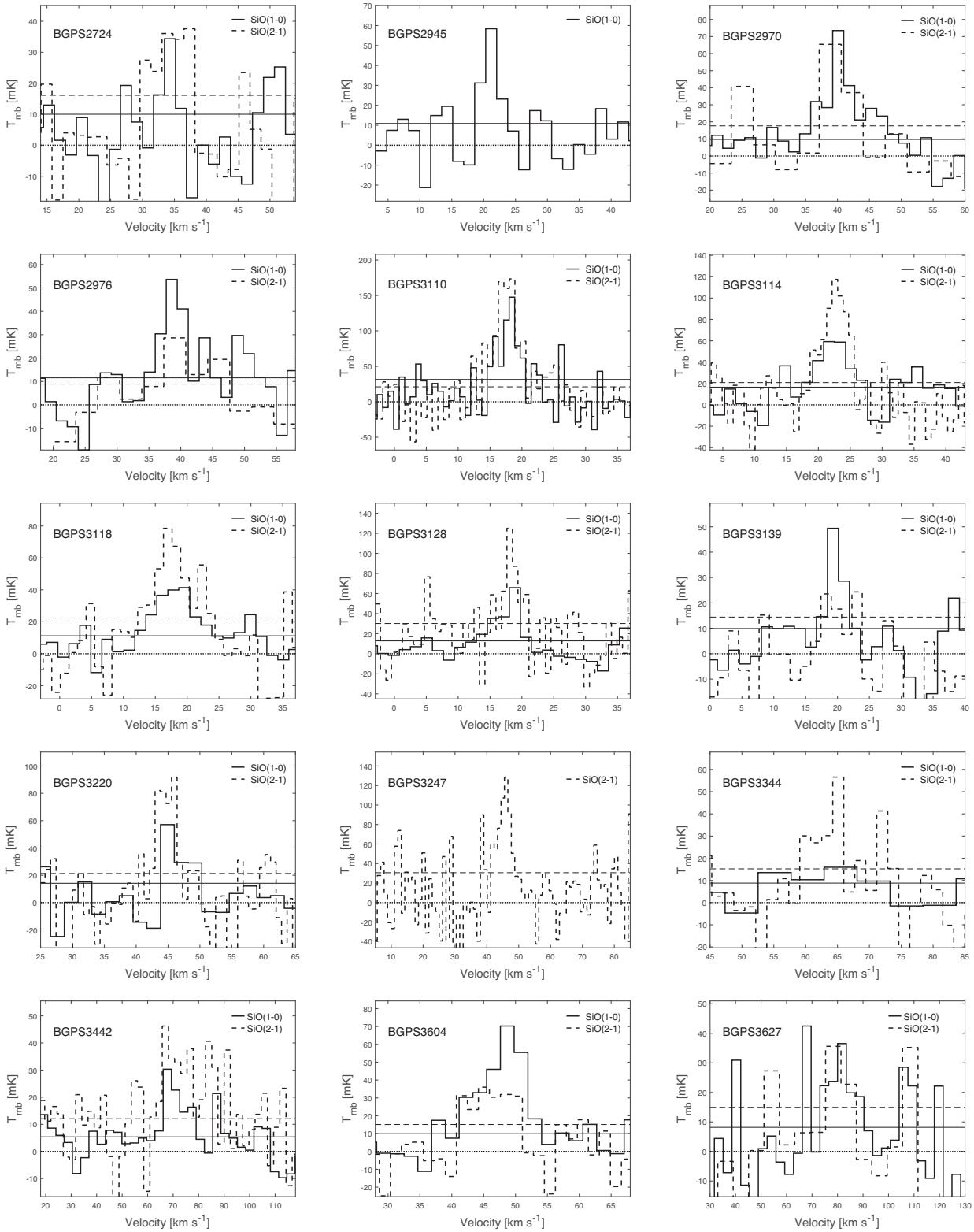

Figure A2. The SiO spectra for individual sources. The solid lines present the SiO 1–0 line profiles and the dashed ones are the SiO 2–1 line profiles. The horizonal solid and dashed lines represent the rms noise levels of the SiO 1–0 and 2–1 lines at the velocity resolutions of these spectra, respectively. The horizonal dotted lines are baselines.

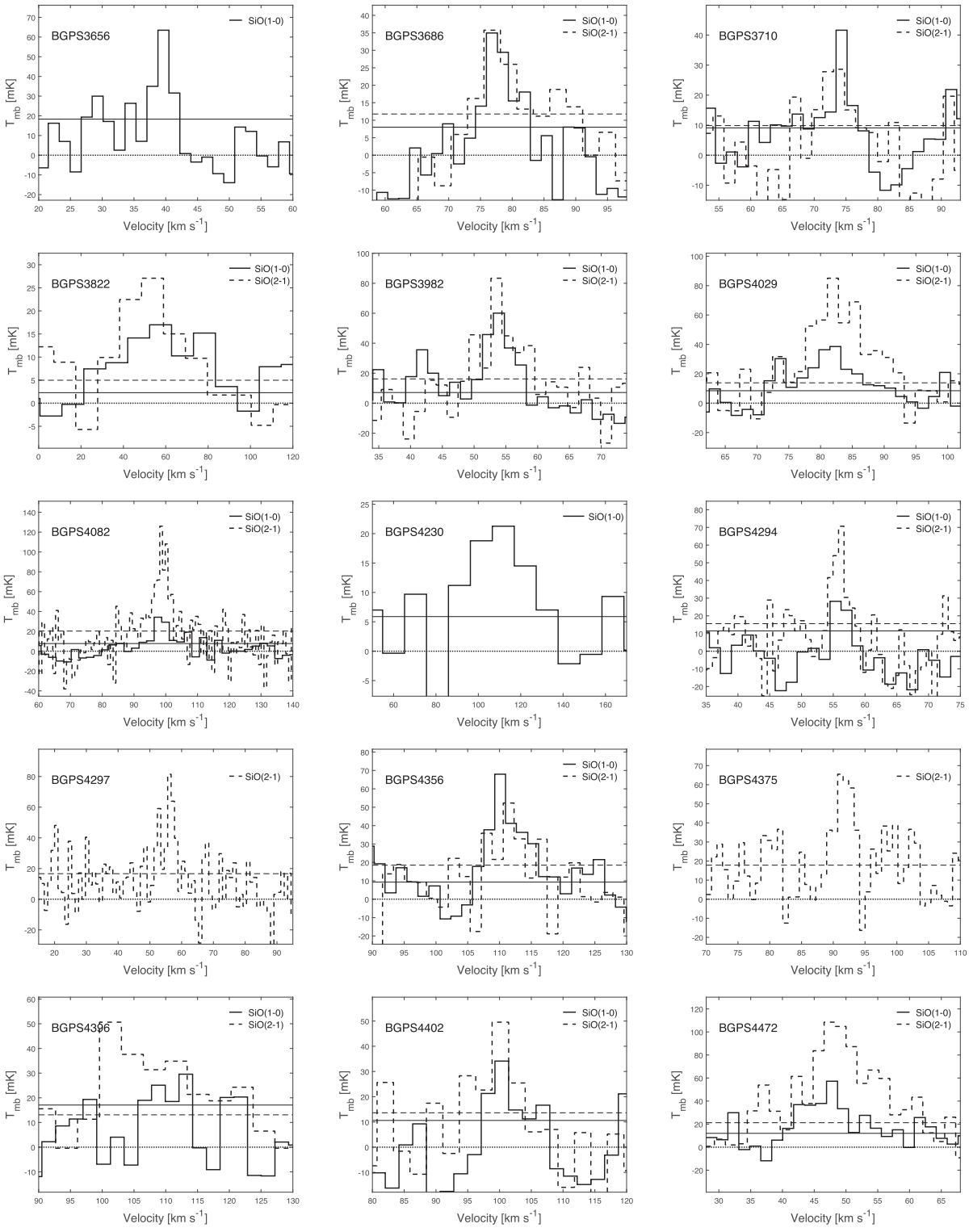

Figure A2 — *continued*

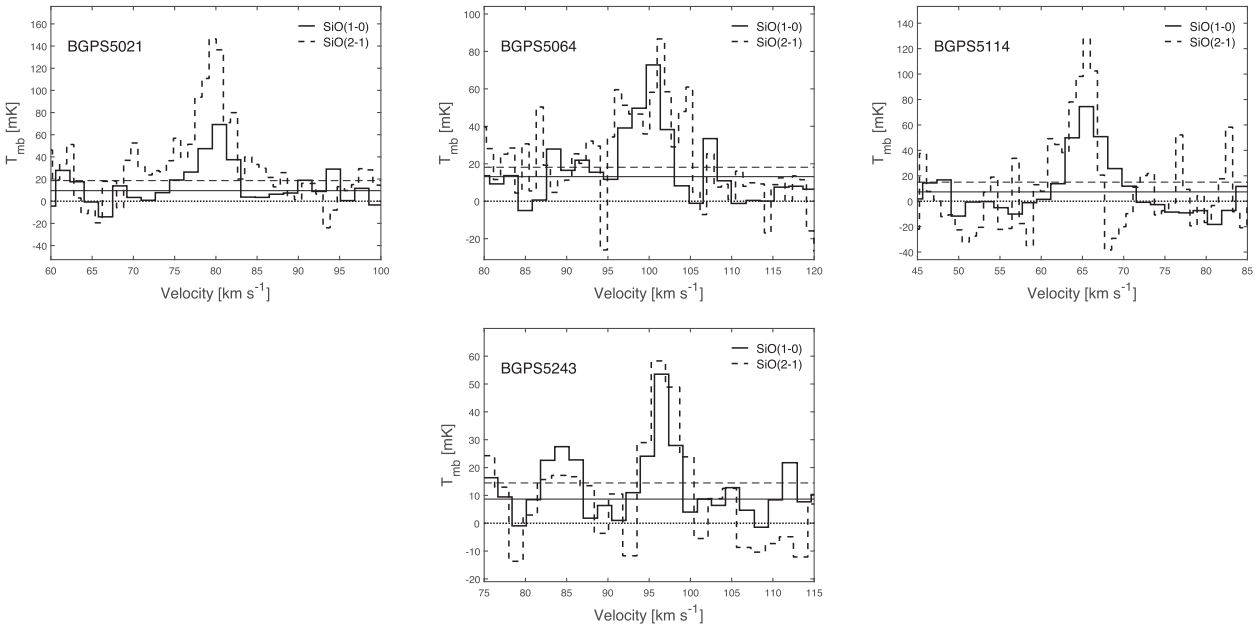

Figure A2 — *continued*

This paper has been typeset from a TEX/LATEX file prepared by the author.